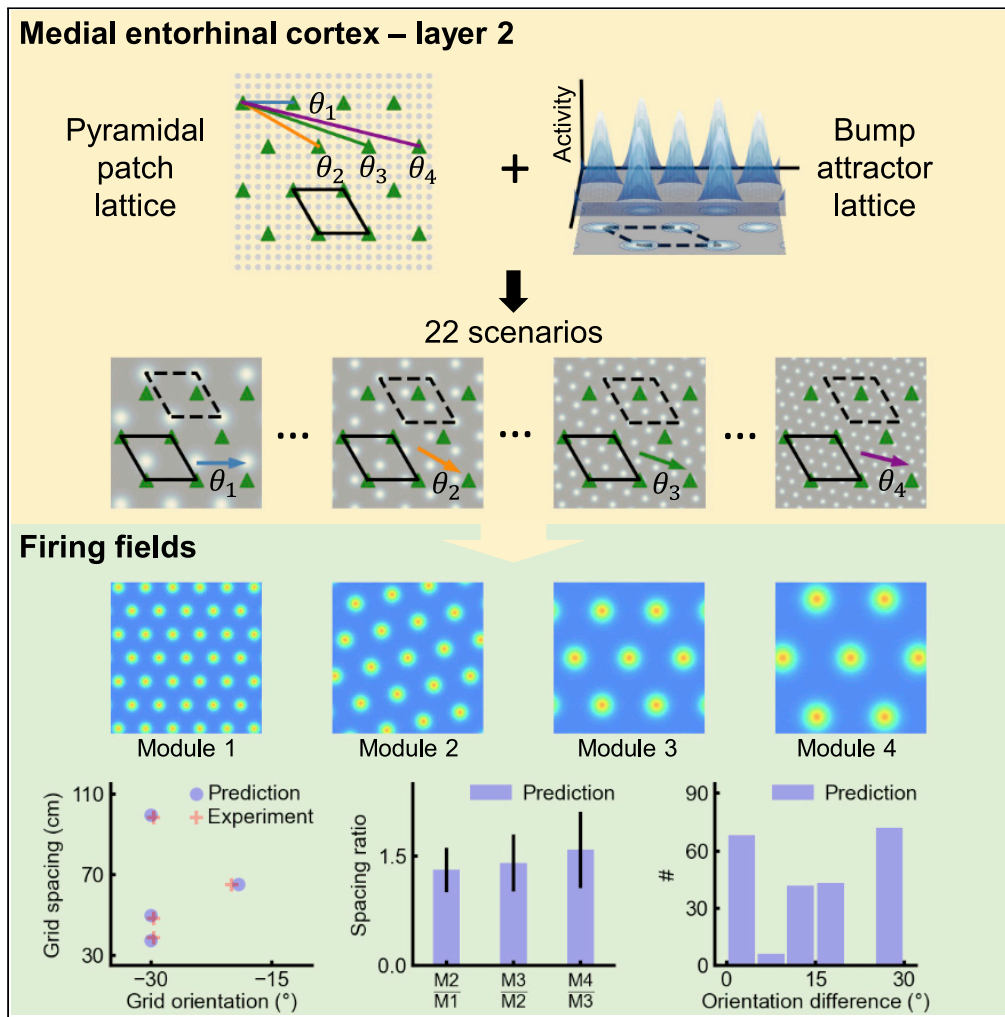


Article

Modularization of grid cells constrained by the pyramidal patch lattice



Tao Wang, Fan Yang, Ziqun Wang, Bing Zhang, Wei Wang, Feng Liu

zhangbing_nanjing@nju.edu.cn (B.Z.)
wangwei@nju.edu.cn (W.W.)
fliu@nju.edu.cn (F.L.)

Highlights

Each module is modeled as a continuous attractor network with specific parameters

The lattice of bump attractors is specifically aligned to the pyramidal patch lattice

Twenty-two scenarios for the bump attractor lattice are proposed

The grid spacing ratios and orientation differences are determined intrinsically



Article

Modularization of grid cells constrained by the pyramidal patch lattice

Tao Wang,¹ Fan Yang,¹ Ziqun Wang,¹ Bing Zhang,^{2,3,*} Wei Wang,^{1,3,*} and Feng Liu^{1,3,4,*}

SUMMARY

Grid cells provide a metric representation of self-location. They are organized into modules, showing discretized scales of grid spacing, but the underlying mechanism remains elusive. In this modeling study, we propose that the hexagonal lattice of pyramidal cell patches may underlie the discretization of grid spacing and orientation. In the continuous attractor network composed of interneurons, stellate and pyramidal cells, the hexagonal lattice of bump attractors is specifically aligned to the patch lattice under 22 conditions determined by the geometry of the patch lattice, while pyramidal cells exhibit synchrony to diverse extents. Given the bump attractor lattice in each module originates from those 22 scenarios, the experimental data on the grid spacing ratio and orientation difference between modules can be reproduced. This work recapitulates the patterns of grid spacing versus orientation in individual animals and reveals the correlation between microstructures and firing fields, providing a systems-level mechanism for grid modularity.

INTRODUCTION

Grid cells in superficial layers of the medial entorhinal cortex (mEC) provide a universal spatial metric via their grid-like firing fields (Doeller et al., 2010; Fyhn et al., 2008; Hafting et al., 2005; Jacobs et al., 2013; Killian et al., 2012; Yartsev et al., 2011). Each grid cell maintains the hexagonally distributed firing fields with specific grid spacing, orientation, and phase (Boccaro et al., 2010; Hafting et al., 2005; Stensola et al., 2015). Grid cells are grouped into modules, and up to four modules have been identified in rats (Stensola et al., 2012); co-modular cells share the grid spacing and orientation but exhibit diverse phases. Modules are numbered with increasing the grid spacing and located from dorsal to ventral mEC (Hafting et al., 2005; Stensola et al., 2012). It is established that grid modularity ensures the precision and scalability of spatial representation (Stemmler et al., 2015; Stensola et al., 2012), responsible for path integration and cognitive maps (Burak and Fiete, 2009; Epstein et al., 2017; Rowland et al., 2016). Accumulating evidence shows that grid modules are also engaged in representing cognitive variables at diverse scales (Bellmund et al., 2018; Constantinescu et al., 2016; Park et al., 2020). All these indicate that modularity has a key role in grid cell functioning.

While the ratios of grid spacing between successive modules roughly fall in the range of 1.4–1.7 (Barry et al., 2007; Gu et al., 2018; Krupic et al., 2015; Stensola et al., 2012) (Table S1), the grid spacing progression exhibits large variability between animals and there seems to be no uniform pattern (Stensola et al., 2012). The grid orientations are also discretized (Stensola et al., 2012) (Table S2); the orientation differences between modules have a preference for 0° and 30° albeit with a few intermediate values (Krupic et al., 2015). It is still challenging to unravel the underlying mechanisms for these scale ratios and orientation differences, as well as module formation.

Continuous attractor network (CAN) models have been proposed to account for firing features of grid cells. Recurrent inhibitory connectivity between principal neurons (Couey et al., 2013), together with external excitatory inputs from the medial septum (Koenig et al., 2011) or hippocampus (Bonnievie et al., 2013), can underlie hexagonally distributed bell-shaped activation bumps on a two-dimensional (2D) neural sheet, and these bumps are able to shift as a whole when animals run in a 2D box (Burak and Fiete, 2009; Fuhs and Touretzky, 2006). This endows the firing fields of individual cells with hexagonal symmetry. Despite the great success of CAN models, the discreteness in grid spacing awaits explanation. Neurons in a CAN have the same grid spacing and orientation, definitely belonging to the same module (Burak and Fiete, 2009; Rowland et al., 2016); but reshaping the profile of recurrent inhibitory connectivity can easily change the scale of firing fields (Burak and Fiete, 2009; Kang and Balasubramanian, 2019), implying that

¹National Laboratory of Solid State Microstructures, Department of Physics, Collaborative Innovation Center of Advanced Microstructures, Nanjing University, Nanjing 210093, P. R. China

²Department of Radiology, Drum Tower Hospital Affiliated to Nanjing University Medical School, Nanjing 210008, P. R. China

³Institute for Brain Sciences, Nanjing University, Nanjing 210023, P. R. China

⁴Lead contact

*Correspondence: zhangbing_nanjing@nju.edu.cn (B.Z.), wangwei@nju.edu.cn (W.W.), fliu@nju.edu.cn (F.L.)

<https://doi.org/10.1016/j.isci.2021.102301>



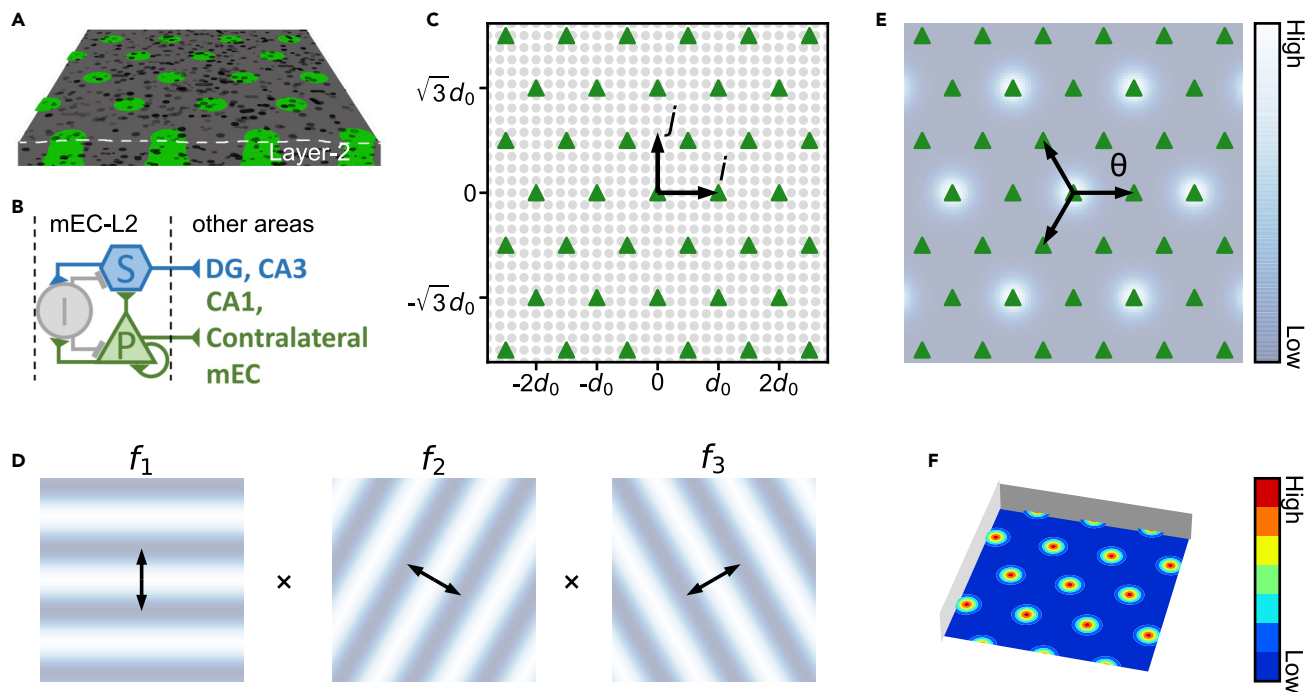


Figure 1. Schematic of the model, activation pattern and firing fields of grid cells

(A) Schematic illustration of principal neurons in mEC-L2. Stellate cells are uniformly distributed, while pyramidal cells gather in patches distributed hexagonally (green).

(B) Schematically shown are connections between different neural types. S: stellate cell; P: pyramidal cell; I: interneuron.

(C) Each module includes 39 hexagonally distributed pyramidal patches (green triangles) and uniformly distributed stellate cells (gray dots) besides interneurons. Each neuron is labeled by its location \mathbf{p} in the i, j -coordinate, where the i -axis parallels the dorsal-ventral axis of mEC-L2.

(D) Activation state of a cell is described by the product of three von Mises functions with distinct orientations. The arrow in each panel denotes the orientation of each function.

(E) Pattern of activity bumps (white) and pyramidal patches (green). θ labels the pattern orientation.

(F) Shown are the firing fields of one grid cell, distributed hexagonally, when an animal ran in a square box. The firing rate is color coded.

See also Figure S1.

the grid spacing of cells might vary continuously. Thus, if we still represent multiple modules using CAN models with distinct parameters, there should exist additional constraints to guarantee the discretized spacing ratios. Such constraints have yet to be identified.

There are two kinds of principal neurons, namely stellate and pyramidal cells; specifically, 10%–20% of pyramidal cells and 11%–40% of stellate cells in mEC-L2 act as grid cells (Boccaro et al., 2010; Gu et al., 2018; Sun et al., 2015; Tang et al., 2016). The CAN models have hardly specified the types of neurons involved; actually, pyramidal cells are distinct from stellate cells in various aspects. In mEC-L2, pyramidal cells gather in patches (with a diameter of 250 μm in mice and 150 μm in rats), which are also distributed hexagonally, whereas stellate cells are uniformly localized beyond the pyramidal patches (Beed et al., 2010; Kitamura et al., 2014; Naumann et al., 2016; Ray et al., 2014) (Figure 1A). Besides broad inhibitory connectivity between principal neurons via interneurons, only pyramidal cells directly send excitatory inputs to other principal neurons (Beed et al., 2013; Couey et al., 2013; Fuchs et al., 2016; Rowland et al., 2018; Zutshi et al., 2018) (Figure 1B). Furthermore, pyramidal cells project primarily to contralateral mEC and sporadically to CA1 of the hippocampus (Beed et al., 2010; Ray et al., 2017; Tang et al., 2016; Varga et al., 2010; Zutshi et al., 2018), whereas stellate cells mainly project to the dentate gyrus (DG) and CA3 (Kitamura et al., 2014; Ray et al., 2014; Rowland et al., 2018; Varga et al., 2010). These findings suggest that stellate and pyramidal cells may serve different functions. The roles for the pyramidal patch lattice in spatial processing are largely unknown.

Inspired by the same symmetry in the architecture of pyramidal patches and grid cell firing fields, here we hypothesize that the pyramidal patch lattice may provide geometrical templates for the arrangement of bump attractors on the neural sheet. We modeled each module by a CAN model and built a large network

of four modules, taking into account the anatomical organizations of stellate and pyramidal cells in mEC-L2. We examined the dynamics of individual modules when the simulated animal ran in a 2D box, and calculated the mutual information (MI) between the animal's position and firing rates of pyramidal cells. By scanning the parameter space, we identified the conditions for neural synchrony and high MI. We explored diverse combinations of four modules and inferred the grid patterns across modules. This study not only quantitatively reproduced experimental observations but also made experimentally testable predictions. Our results suggest that modular organization of grid cells is dictated by the pyramidal patch lattice.

RESULTS

Network model and firing fields of neurons

It was found early that grid cells with similar phases are close to each other anatomically (Hafting et al., 2005; Heys et al., 2014) and was revealed recently that they are localized according to their phases within a module—map-like organization (Gu et al., 2018). A hexagonal lattice of activated neural ensembles is observable, as the CAN model has predicted (Burak and Fiete, 2009). Although our work is based on the CAN model, we did not investigate the temporal evolution of membrane potential or gating variables of neurons, rather assuming that the network can admit bump attractors given proper synaptic connectivity and inputs. That is, a phenomenological model is adopted here.

The network model was constructed as follows. Pyramidal patches are located at vertexes of a hexagonal lattice, while stellate cells are distributed uniformly between them (Figure 1C). Interneurons located around these principal neurons mediate inhibitory interactions. As the pyramidal patch lattice is intact in mEC-L2 (Ray et al., 2014), it provides a natural reference for describing the locations of neurons. The lattice axis parallel to the dorsal-ventral axis of mEC is defined as i -axis, and j -axis is vertical to the i -axis. The physical distance between two adjacent pyramidal patches is defined as the unit length d_0 for convenience, which is around 300 μm for mice (Gu et al., 2018) but is unknown for rats. Each neuron is marked by $\mathbf{p} = (i, j)$ in this i, j -coordinate. From the dorsal to ventral, neurons are organized into distinct modules. Within each module, stellate and pyramidal cells are supposed to be connected recurrently and obey the attractor dynamics. As we focused on the relationship between individual modules and the pyramidal patch lattice, ignoring the correlation between different modules, it was unnecessary to construct a uniform coordinate system across modules. The coordinate origin for each module was separately set to be at the position of the most central patch.

As the exact number of patches per module is unknown, we assumed that each module included 39 pyramidal patches unless otherwise specified; their locations are shown in Table S3. Thirty-nine patches is an acceptable estimate. First, it was reported that the total number of patches is 69–115, varying markedly across species (Naumann et al., 2016); four modules were identified in mEC-L2 of rats, and different modules are heavily overlapped (Stensola et al., 2012). Thus, each module contains dozens of patches. Second, the area of each module in mEC-L2 is on the order of square millimeters, also allowing for tens of patches (Ray et al., 2014; Stensola et al., 2012). Third, 39 patches cover 7 rows with 5 or 6 patches per row, which is convenient for demonstration and analysis. Furthermore, one patch comprises 111–837 pyramidal cells, depending remarkably on species (Naumann et al., 2016). Notably, not all pyramidal cells behave as grid cells; only those at the patch edges have relatively high grid scores (Gu et al., 2018). As we concentrated on the hexagonal lattice of pyramidal patches rather than details of each patch, we assumed that each patch comprised one representative pyramidal cell unless otherwise specified. We also explored other cases wherein the patch lattice was distorted by deviating vertexes from ideal positions, or defects were introduced by discarding vertexes randomly.

We turned to investigate the firing activity of grid cells. Owing to the topographic organization of grid cells (Gu et al., 2018; Hafting et al., 2005; Heys et al., 2014), the firing rate of each cell depended on its location \mathbf{p} , with a hexagonal symmetry on the neural sheet, and was assumed to obey

$$f(\mathbf{p}, t) = F_{\text{Max}} \cdot f_1(\mathbf{p}, t) \cdot f_2(\mathbf{p}, t) \cdot f_3(\mathbf{p}, t),$$

$$f_n(\mathbf{p}, t) = \exp\left(\kappa \cdot \left(\cos\left(\frac{4\pi(\mathbf{p} - \mathbf{p}_{\text{Max},n}(t)) \cdot \mathbf{u}_n}{\sqrt{3}D}\right) - 1\right)\right), n = 1, 2, 3. \quad (\text{Equation 1})$$

F_{Max} is the maximal firing rate, and f_1, f_2, f_3 are von Mises functions with different orientations (Stemmler et al., 2015), used to generate hexagonally arranged bumps (Figures 1D and 1E). How the regular bump lattice is formed is illustrated in Figures S1A–S1I. $\mathbf{p}_{\text{Max},1}(t)$, $\mathbf{p}_{\text{Max},2}(t)$ and $\mathbf{p}_{\text{Max},3}(t)$ signify the neurons with the highest firing rate (i.e., zero phase) at time t ; for simplicity, they were all set to $\mathbf{p}_{\text{Max}}(t)$, which is the center

of a bump attractor (other bump attractors are periodically repeated). \mathbf{u}_1 , \mathbf{u}_2 , \mathbf{u}_3 are unit vectors spaced 120° apart, characterizing the orientations of patterns in f_1 , f_2 , and f_3 , respectively (Figure 1D). Given that zero phase lines are vertical to \mathbf{u}_n and the equivalence of \mathbf{u}_1 , \mathbf{u}_2 and \mathbf{u}_3 , we introduced θ , defined as the orientation of zero phase lines for f_1 , to label the orientation of the activation bump lattice for simplicity (Figure 1E). D equals the bump spacing, while κ scales the bump extension. In biophysically realistic CAN models, the values of F_{Max} , θ , D , and κ would depend on boundary conditions of the neural sheet, profiles of recurrent synaptic connectivity and the strength of external input (Burak and Fiete, 2009). Here they were just predetermined as parameters (Table S4). Specifically, θ and D were taken as free parameters in simulation.

We could directly manipulate $\mathbf{p}_{\text{Max}}(t)$ to model the shift of activation bumps following the animal's movement in the x , y -coordinate of the box (see transparent methods):

$$\begin{cases} \frac{dp_{\text{Max},i}(t)}{dt} = \alpha \frac{dx}{dt} = \alpha \cdot s(t) \cdot \cos(\phi(t)) \\ \frac{dp_{\text{Max},j}(t)}{dt} = \alpha \frac{dy}{dt} = \alpha \cdot s(t) \cdot \sin(\phi(t)), \end{cases} \quad (\text{Equation 2})$$

where $p_{\text{Max},i}(t)$ and $p_{\text{Max},j}(t)$ denote the i , j -component of $\mathbf{p}_{\text{Max}}(t)$, respectively. The x -axis (y -axis) corresponds to the animal's running direction when the bumps shift along the i -axis (j -axis) (Burak and Fiete, 2009; Fuhs and Touretzky, 2006). $\phi(t)$, denoting the shift direction, takes the same amplitude as the animal's motion direction $\psi(t)$. α is a constant in units of $d_0 \text{ m}^{-1}$, controlling the shift scale of activation bumps, and $s(t)$ is the animal's running speed. $\alpha s(t)$ thus represents the shift rate of activation bumps. Consequently, a 1-meter movement along the x -axis in the box corresponds to a shift of α along the i -axis in the activation pattern. When the simulated animal ran continuously in the box, the path of one bump's center was mapped to the animal's trail (Figures S1J–S1L).

To simulate the spiking dynamics of each cell, independent Poisson random variables were generated with mean of $f(\mathbf{p}, t)\Delta t$ at time t , representing the spike count between t and $t + \Delta t$. When monitoring the cell's discharge, the animal's position was recorded simultaneously to plot a spike count map; after each trial, this map was used to produce a firing map as was done experimentally (Hafting et al., 2005) (see transparent methods). Further, the averaging over 100 trials could yield hexagonally distributed firing fields (Figure 1F). Taken together, our model can capture two fundamental features of grid cells: neural activation bumps are centered on a hexagonal lattice, shifting in response to the animal's motion (Burak and Fiete, 2009; Fuhs and Touretzky, 2006; Gu et al., 2018), and firing fields of cells are hexagonally distributed, anchored to the environment (Hafting et al., 2005; Krupic et al., 2015).

Synchronous spiking of pyramidal cells in individual modules

It is generally accepted that neurons in the same activation bump discharge synchronously in the attractor network (Compte et al., 2000; Xue and Liu, 2014). The CAN model of grid cells can admit dozens of hexagonally distributed bumps simultaneously (Burak and Fiete, 2009; Fuhs and Touretzky, 2006; Gu et al., 2018). It is unclear how synchronous firings in each bump are correlated within a module. Here, we first explored the firing dynamics in individual modules when the simulated animal ran on a linear track at a constant rate of 0.6 m/s. The module dynamics depended remarkably on the free parameters θ and D . For most values of θ and D , the hexagonal lattice of activation bumps was of arbitrary spacing and orientation, mismatching the pyramidal patch lattice (Figure 2A, top); accordingly, pyramidal cells in different patches had distinct activation phases and discharged asynchronously (Figure 2B, top). Note that each spike train was produced according to the firing rate, obeying a Poisson distribution. By contrast, when the bump attractor lattice matched the patch lattice for specific values of θ and D , all pyramidal cells had the same activation phase (Figure 2A, bottom) and almost spiked synchronously (Figure 2B, bottom).

When the animal ran freely in a 2D box, the spike map of each cell was obtained by monitoring their spiking and recording the animal's location simultaneously. Pyramidal cells had similar spike maps if they discharged synchronously, and their centers of spiking clusters overlapped (Figure 2C). Moreover, their firing rates varied nearly periodically when the animal ran along a definite direction (Figure 2D). These results were in sharp contrast to those in the case of asynchronous spiking. Notably, the activation phases of stellate cells were always continuously distributed in both the cases, and their spiking clusters scattered on the plane (Figure S2A).

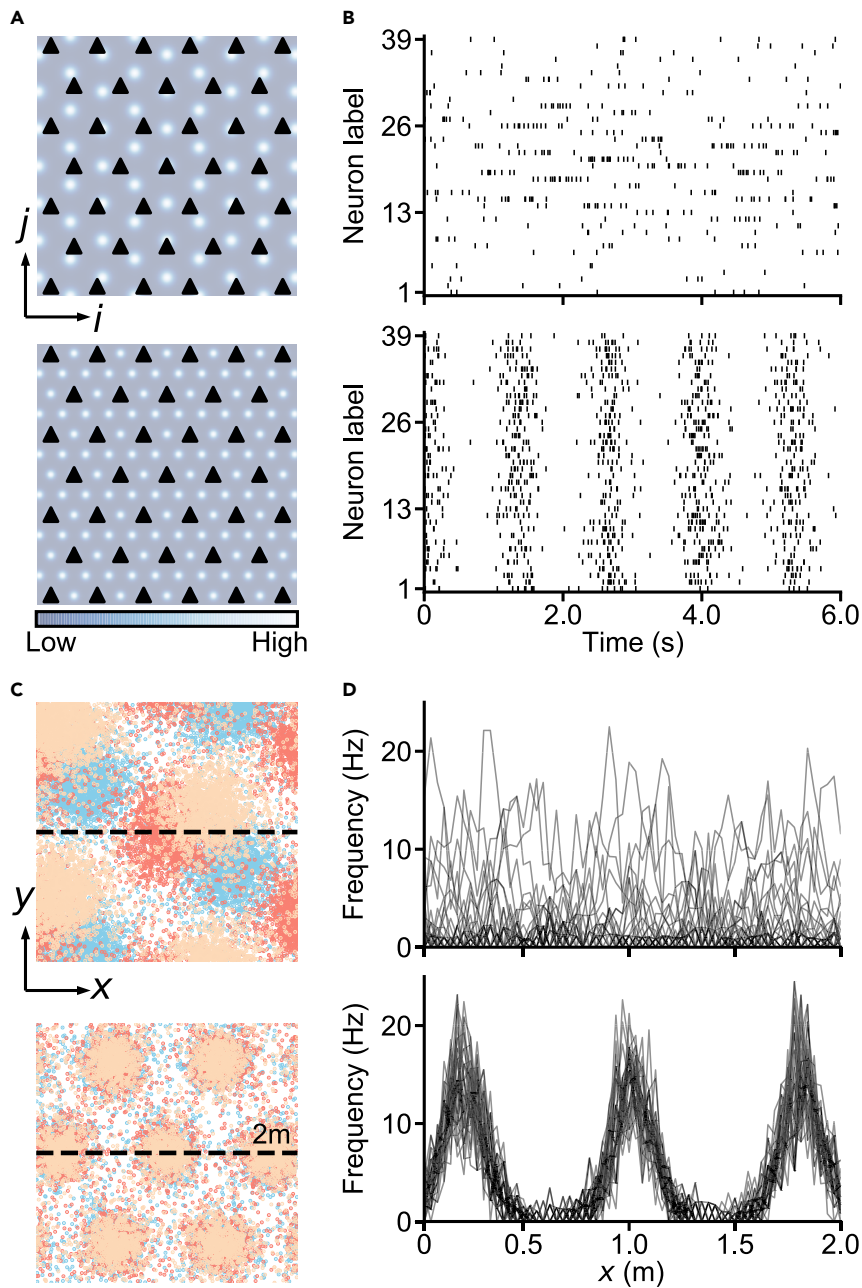


Figure 2. Discharge of pyramidal cells under diverse conditions

(A) Snapshots of the activation pattern relative to the pyramidal patch lattice when the animal ran rightward on a linear track. White areas: centers of bump attractors; black triangles: pyramidal patches. Firing activity is represented by heatmap. Top panel: $\theta = 30^\circ$ and $D = 0.8d_0$; bottom panel: $\theta = 0^\circ$ and $D = 0.5d_0$ (here and thereafter).

(B) Raster plots of all pyramidal cells.

(C) Spike maps of three representative pyramidal cells when the animal ran freely in the 2D square box. Each dot represents a spike, and different colors denote distinct cells. The animal's path is not shown.

(D) Firing rates of 39 pyramidal cells versus the position along the dashed line in (C) on a trial.

See also [Figure S2](#).

One way to quantify the extent of neural synchrony is measuring the MI between the animal's position and firing rates of all pyramidal cells (see [transparent methods](#)). This method is superior to calculating the spatial or temporal correlation between neural pairs, since the latter characterizes a local rather than global

coherence. Moreover, the MI reflects the spatial information contained in the population activity (Domnisoru et al., 2013) and is positively correlated with the performance of population decoding. In the following, we always used the MI to represent the synchrony of pyramidal cells. Strong synchrony was associated with a high MI: 0.75 bits versus 0.01 bits under conditions of synchronous and asynchronous firing, respectively (Figures 2D and S2B). This result can be intuitively understood as follows. The firing activity of each cell is defined as high or low according to whether the animal is within its firing field or not. Given the in-field state of cells as state 1 and out-of-field state as state 0, 1 bit of information could be acquired from the spiking activity of a cell if the probabilities of being in state 0 and state 1 are equal. This tells whether the animal is within firing fields although its exact location in the 2D box might be unknown. This information is well maintained with synchronous firing, whereas it is blurred in the presence of asynchronous firing. Overall, the pyramidal patch lattice seems to provide a template for evoking synchronous firing.

Requirements for synchronous firing of pyramidal cells

To specify the geometrical constraint on the activation bump lattice by the pyramidal patch lattice, here we systematically changed parameters to identify conditions leading to synchronous firing of pyramidal cells. In the plane spanned by the orientation and normalized spacing of the activation bump lattice, there existed a few areas associated with relatively high MI (Figure 3A); the corresponding $|\theta|$ was localized around four orientations θ_i ($i = 1 - 4$), which were separately parallel to the lines connecting neighboring pyramidal patches, i.e., $\theta_1 = 0^\circ$, $\theta_2 = 30^\circ$, $\theta_3 = \arcsin\left(\frac{\sqrt{3}}{2\sqrt{7}}\right) \frac{180^\circ}{\pi} \approx 19^\circ$ and $\theta_4 = \arcsin\left(\frac{\sqrt{3}}{2\sqrt{13}}\right) \frac{180^\circ}{\pi} \approx 14^\circ$ (with the corresponding distances $d_1 = d_0$, $d_2 = \sqrt{3}d_0$, $d_3 = \sqrt{7}d_0$, and $d_4 = \sqrt{13}d_0$) (Figure 3B). Meanwhile, D had to take specific values for high MI. Thus, to reach a high MI the activation bump lattice should be aligned to the patch lattice in some special manner.

Choosing one of the four specific orientations, we probed how the MI varied with D (Figure 3C). Here, D was restricted in the range of $0.18d_0 - 1.1d_0$ as explained later. For each orientation, there appeared several major and minor peaks. At $\theta = \theta_1$, five major peaks arose at d_0 , $\frac{d_0}{2}$, $\frac{d_0}{3}$, $\frac{d_0}{4}$, and $\frac{d_0}{5}$ (called cases 1a-1e) and four minor peaks at $\frac{2d_0}{3}$, $\frac{2d_0}{5}$, $\frac{2d_0}{7}$, and $\frac{2d_0}{9}$ (called cases 1f-1i). Note that case 1b corresponds to the example with synchronous spiking shown in Figure 2. Peak locations and their naming for all cases are presented in Table 1. There were 22 MI peaks in total, and they were classified as primary, secondary or tertiary ones.

The type of MI peak was closely correlated with the geometrical relation between the pyramidal patch and activation bump lattices. For (θ, D) admitting a primary MI peak, the activation bump lattice could match the pyramidal patch lattice perfectly, i.e., a rhombus on the bump lattice was congruent with the rhombic cellular of the patch lattice, with the side length being d_0 (Figures 3D and S3). Thus, the ratio of the total number of bumps to that of patches, ρ , was an integer (Table 1), and all pyramidal cells could discharge synchronously, leading to the MI of around 0.7 bits (Figures 3E and S3). For (θ, D) admitting a secondary MI peak (i.e. cases 2c-2g), the bump lattice partially matched the patch lattice, with the side length of the matching rhombus equaling d_2 . Thus, ρ equaled $4/3$, $16/3$, $25/3$, $49/3$, and $64/3$, respectively, and pyramidal cells were classified as three subgroups, within which they spiked synchronously and had the same firing maps. Note that the number of subgroups was equal to the denominator of ρ and the corresponding MI was roughly one-third of 0.7 bits. For the other cases, the match between the bump lattice and patch lattice was further weakened, with the side length being $2d_1$; the denominator of ρ was 4, and pyramidal cells were divided into four subgroups. The MI in these cases was around one-fourth of 0.7 bits.

Further analysis revealed that the MI peak height depended greatly on the extent to which the activation bump lattice geometrically matched the pyramidal patch lattice, rather than on the number of patches or the shape of module boundary (Figures S4A–S4F). Theoretically, there was no constraint on the range of D in our model. However, it was impossible to maintain an incredibly small bump spacing, i.e. $D < 0.2d_0$, according to numerical simulation of the detailed CAN model (Burak and Fiete, 2009). No more primary peaks appeared at $D > d_0$ in all the MI curves (Figure S4G). It was also reported that the bump spacing in mice is 60–260 μm , less than d_0 (Gu et al., 2018) (no such data are available for rats). Thus, D was constrained between $0.18d_0$ and $1.1d_0$.

So far, one patch contains only one pyramidal cell, and all patches neatly line up, forming an ideal hexagonal lattice. Actually, one patch comprises much more pyramidal cells (Brecht et al., 2014; Naumann et al.,

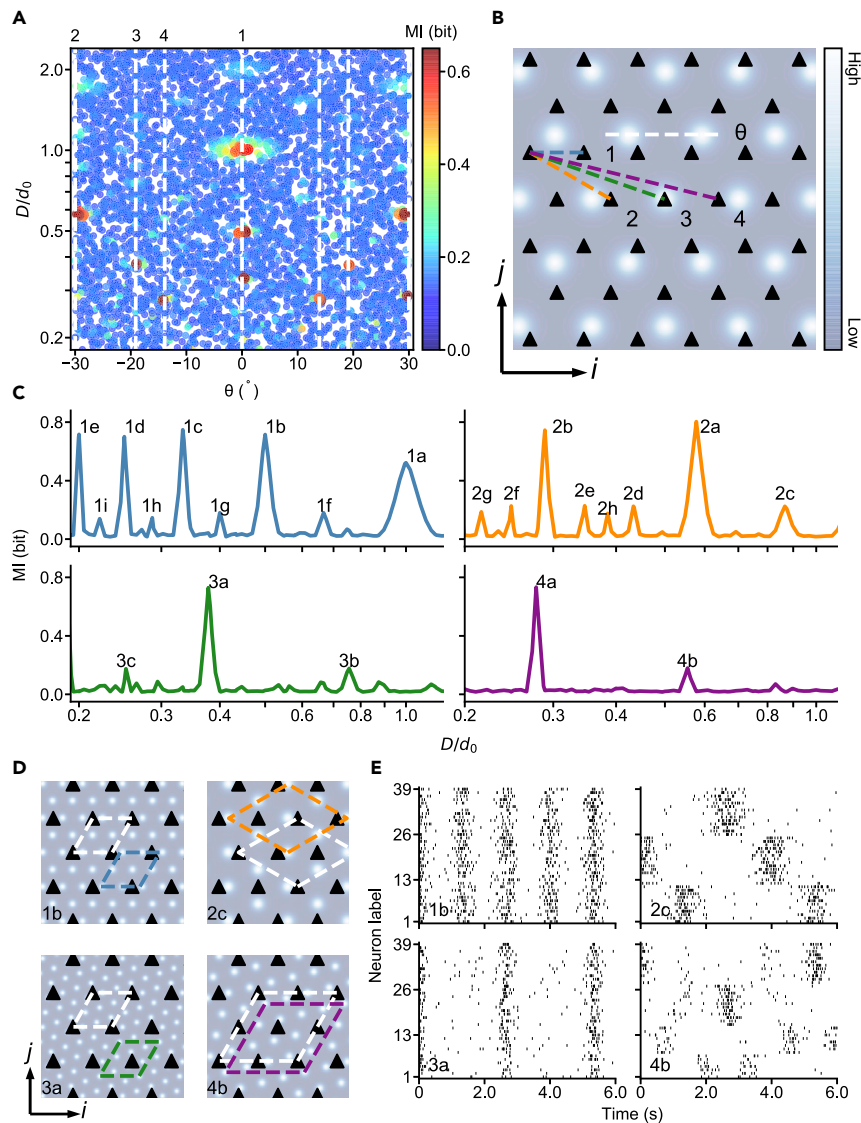


Figure 3. Conditions for acquiring high mutual information (MI)

(A) Heatmap of the MI as a function of the normalized spacing and orientation of the activation bump lattice. Larger dots correspond to MI > 0.5 bits. D -axis is in log scale, and d_0 denotes the physical distance between neighboring pyramidal patches.

(B) Shown are four representative orientations of the activation pattern, labeled by colored dashed lines.

(C) The MI versus D for different θ , with the same color code as in (B). D -axis is in log scale. There exist 22 peaks in total, including 9 primary peaks.

(D) Relations between the activation bump lattice and the pyramidal patch lattice under four representative conditions. Marked are two minimal matching units of the activation pattern (colored rhombus) and the patch lattice (white rhombus). The same notation is used as in (C).

(E) Spatiotemporal firing patterns of pyramidal cells under the four conditions in (D). Neurons are sorted according to their synchrony.

See also [Figures S3](#) and [S4](#).

2016), and patches may deviate from their ideal locations (distortion) or even get lost (defect) (Ray et al., 2014). We found that those MI peaks were largely robust against the change in patch size, distortion and defect of the lattice over a certain range (Figures S4H–S4J). Collectively, we identify 22 pairs of (θ, D) , around which pyramidal cells can exhibit synchrony to diverse extents, with each allowing for a specific alignment of the bump lattice to the pyramidal patch lattice.

Table 1. Essential features of 22 scenarios with MI peaks

	Case	$\theta(^{\circ})$	D/d_0	ρ	Case	$\theta(^{\circ})$	D/d_0	ρ
Primary peak	1a	0	1	1	2a	-30	$\sqrt{3}/3$	3
	1b	0	1/2	4	2b	-30	$\sqrt{3}/6$	12
	1c	0	1/3	9	3a*	-19	$\sqrt{7}/7$	7
	1d	0	1/4	16	4a*	-14	$\sqrt{13}/13$	13
	1e	0	1/5	25				
Secondary peak	2c	-30	$\sqrt{3}/2$	4/3	2f	-30	$\sqrt{3}/7$	49/3
	2d	-30	$\sqrt{3}/4$	16/3	2g	-30	$\sqrt{3}/8$	64/3
	2e	-30	$\sqrt{3}/5$	25/3				
Tertiary peak	1f	0	2/3	9/4	2h	-30	$2\sqrt{3}/9$	27/4
	1g	0	2/5	25/4	3b*	-19	$2\sqrt{7}/7$	7/4
	1h	0	2/7	49/4	3c*	-19	$2\sqrt{7}/21$	63/4
	1i	0	2/9	81/4	4b*	-14	$2\sqrt{13}/13$	13/4

*Note that the orientations for 3- and 4-labeled cases were actually $-\arcsin\left(\frac{\sqrt{3}}{2\sqrt{7}}\right) \times \frac{180^{\circ}}{\pi}$ ($\approx -19^{\circ}$) and $-\arcsin\left(\frac{\sqrt{3}}{2\sqrt{13}}\right) \times \frac{180^{\circ}}{\pi}$ ($\approx -14^{\circ}$) respectively.

Discretized modules of grid cells

The results above raise the possibility that synchronous firing of pyramidal cells may be engaged in spatial representation and the activation bump lattice in individual modules may derive from the 22 scenarios above. Indeed, synchronous firing has been recorded in mEC, involved in spatial navigation (O'Neill et al., 2017) and development of specific cell types (Dawitz et al., 2020; Unichenko et al., 2015). To test this idea, we need infer the firing fields of grid cells and make comparison with existing experimental data. Meanwhile, we sought to unravel the principle for modular organization in a large network of mEC-L2; mostly, the network comprised four modules. Under this supposition, each module was represented by a pair (D, θ) , one of the 22 pairs in Table 1 (i.e., $(D, \theta) \in \{(D_{1a}, \theta_{1a}), (D_{1b}, \theta_{1b}), \dots, (D_{4b}, \theta_{4b})\}$), and modules were numbered with increasing the bump scale in each combination of multiple modules.

We first derived the grid spacing ratios and orientation differences between modules. According to Equation (2), the firing fields of a cell were related to the activation bump lattice as follows (see also Figures S1J–S1L). For a neuron in module m characterized with (D_m, θ_m) , its grid spacing S_m and orientation O_m equaled D_m/α and θ_m , respectively. Another neuron was from module n characterized with (D_n, θ_n) . Since α was the same for all modules of an animal as shown later, their spacing ratio and orientation difference were separately

$$\frac{S_m}{S_n} = \frac{D_m/\alpha}{D_n/\alpha} = \frac{D_m}{D_n}, \quad (\text{Equation 3})$$

$$|O_m - O_n| = |\theta_m - \theta_n|. \quad (\text{Equation 4})$$

Thus, both the grid spacing ratio and orientation difference between two modules were determined by the features of hexagonal bump lattices involved, which were conferred by the pyramidal patch lattice as shown previously.

We then calculated the spacing ratios and orientation differences for all possible combinations of modules. Given each module characterized with (D, θ) from the 22 pairs, we explored all ($C_{22}^4 = 7315$) combinations of four modules and calculated the spacing ratios between successive modules within each combination using Equation (3). We got 1.32 ± 0.31 , 1.41 ± 0.39 , and 1.59 ± 0.52 (mean \pm s.d., here and elsewhere) for S_2/S_1 , S_3/S_2 , and S_4/S_3 , respectively, which roughly agreed with the data from four-module measurement (Stensola et al., 2012), as well as other experimental observations (Barry et al., 2007; Gu et al., 2018; Krupic et al., 2015) (Figure 4A). We also calculated the orientation difference between any two modules using Equation (4). The histogram showed two peaks at 0° and 30° , as well as some intermediate values (Figure 4B), consistent with the experimental result (Krupic et al., 2015). Such agreements support our speculation about the representation of activation bump lattices among the 22 scenarios.

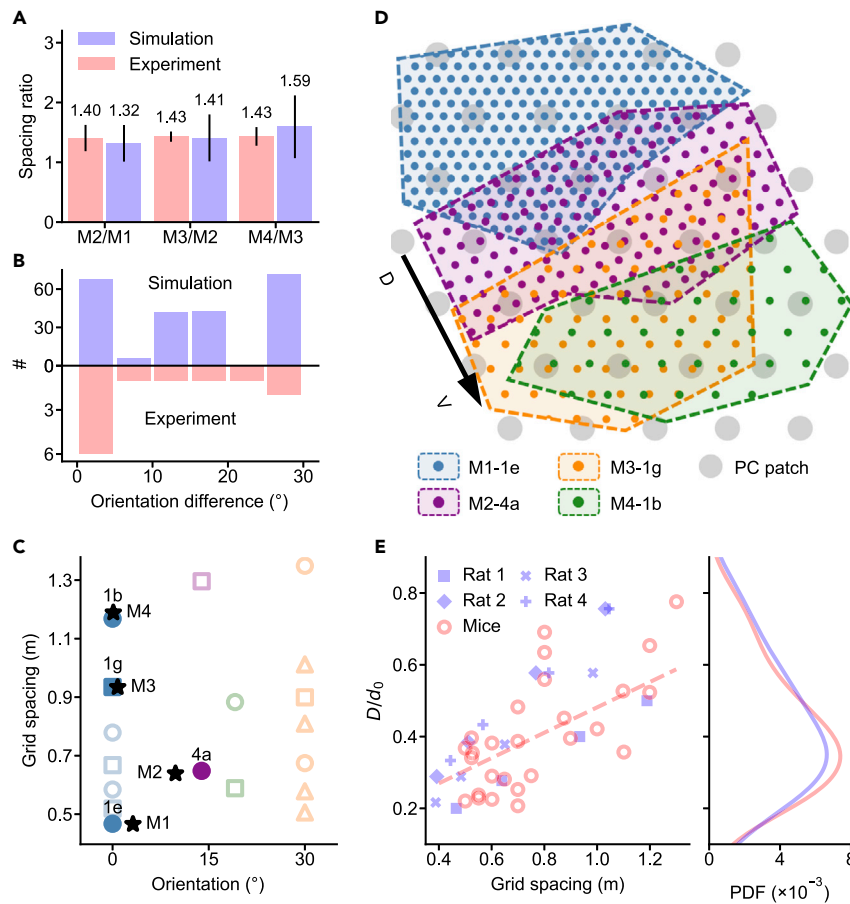


Figure 4. Discretized modules of grid cells

(A) Mean ratios of grid spacing between successive modules. Red bars denote experimental data from [Stensola et al. \(2012\)](#), while blue bars represent the average over all 7315 combinations of 4 modules from the 22 scenarios. Error bars represent the standard deviations.

(B) Distribution of grid orientation difference between two modules. Top, simulation results; bottom, experimental data from [Krupic et al. \(2015\)](#).

(C) Grid spacing and orientations of four modules for rat 1: experimental data from [Stensola et al. \(2012\)](#) (black star) and estimates (solid). Open symbols represent the estimates for other cases from the 22 scenarios; circle, triangle and square correspond to the cases featuring a primary, secondary or tertiary MI peak, respectively.

(D) Schematic of modular organization of grid cells in mEC-L2 of rat 1. Different colors label distinct modules. The colored shadow, colored dots and gray circles separately represent grid cells, centers of activation bumps and pyramidal patches. The boundary of each module is arbitrary. Note that the alignment of bump lattices to the patch lattice is based on our simulation results.

(E) Shown are the bump spacing versus grid spacing (left) and probability density function (PDF) versus the bump spacing (right). Left: Red circles denote the data from mice in [Gu et al. \(2018\)](#), while the red dashed line is a fit to the data with $p = 3.4 \times 10^{-5}$ and $R^2 = 0.48$. The bump spacing was normalized by $d_0 = 300 \mu\text{m}$. Blue symbols denote the data for rats: the grid spacing was obtained experimentally, while the bump spacing was an estimate. Right: The red and blue solid lines represent the data from mice and rats, respectively. The probability density is the kernel density estimate with Scott's rule. See also [Figure S5](#).

We further estimated the spacing and orientations of activation bump lattices according to the experimental recordings of grid spacing and orientation in individual animals, $M_R = \{(S_1, O_1), (S_2, O_2), (S_3, O_3), (S_4, O_4)\}$. Although multiple empirical studies ascertained more than one grid module in individual animals ([Barry et al., 2007](#); [Gu et al., 2018](#); [Krupic et al., 2015](#); [Stensola et al., 2012](#)), only four rats were reported to comprise four modules ([Stensola et al., 2012](#)). For each such rat (rats 1–4 in [Table S2](#)), we identified a combination C_E of four modules such that C_E was most associated with M_R in terms of both the spacing ratios and orientation differences between modules (see [transparent methods](#) and [Figures S5A](#) and [S5B](#)). For example, $C_{E1} = C(1e, 4a, 1g, 1b) = \{(D_{1e}, \theta_{1e}), (D_{4a}, \theta_{4a}), (D_{1g}, \theta_{1g}), (D_{1b}, \theta_{1b})\}$ was the most possible

correspondence of the M_{R1} for rat 1; accordingly, the average ratio of the bump to grid spacing equaled $d_0/2.34 \text{ m}^{-1}$ - estimate for α . Once α was known, we in turn obtained the estimate of grid spacing via dividing D by α . The estimates for rat 1 are shown in Figure 4C, while those for rats 2–4 are displayed in Figure S5C. Most of the estimates coincided well with the experimental data. Such high consistency in pairwise comparison further suggests the rationality behind our speculation.

On basis of these estimates, we could infer the maximal number of grid modules. Of note, three, two, three, and two of four modules, respectively, for rats 1–4 were characterized with (D, θ) featuring a primary MI peak in Figure 3C, indicating that the 22 scenarios could be involved in spatial representation to distinct extents. Diverse combinations of modules may yield different spacing ratios and orientation differences from the existing data, which awaits experimental validation. Possibly, only some scenarios could be engaged and the others should be excluded for specific animals, which may be related to other mechanisms; for instance, it was reported that the best decoding performance was achieved when the spacing ratio was close to 1.5 (Stemmler et al., 2015). Indeed, all the spacing ratios recorded experimentally ranged from 1.25 to 1.51 for rats 1–4, and the mean was around 1.36, according to which we were able to predict the maximal number of grid modules. For fixed spacing ratio of 1.5, there might be 5 ($\approx 1 + \log_{1.5} \frac{d_0}{0.2d_0}$) modules with D ranging from $0.2d_0$ to d_0 . For fixed spacing ratio of 1.36, there could be 6 ($\approx 1 + \log_{1.36} \frac{d_0}{0.2d_0}$) modules. Alternatively, considering that there were separately 16, 12, 17, and 11 cases available for rats 1–4 (each with the grid spacing in the range of S_1 – S_4 ; see Figures 4C and S5C), the average usage rate per case was roughly $\left(\frac{4}{16} + \frac{4}{12} + \frac{4}{17} + \frac{4}{11}\right) / 4 \approx 0.295$. Consequently, the maximal number of grid modules could be 6 ($\approx 22 \times 0.295$).

Integrating the results above, we illustrated four grid modules together relative to the pyramidal patch lattice to depict the modular organization (for rat 1 in Figure 4D and for rats 2–4 in Figure S5D). There were four common features. First, grid cells in each module were organized as a topographic map (Gu et al., 2018; Hafting et al., 2005; Heys et al., 2014). Second, four modules were located from the dorsal to ventral with increasing the grid spacing (Hafting et al., 2005; Stensola et al., 2012). Third, the activation bump lattice in each module was governed by the pyramidal patch lattice. Fourth, the grid spacing was proportional to the bump spacing for each rat, with S/D in the range of 1.35–2.34 m/d_0 . This linear relationship was also observable in mice; Figure 4E shows both the estimated bump spacing versus the grid spacing measured from four rats and the bump spacing versus grid spacing recorded from mice (Gu et al., 2018). Furthermore, the probability distribution of estimated bump spacing for rats was highly consistent with that for mice. These results suggest that rats and mice may have similar preference for grid patterns across modules.

Reliability of estimation

Here, we further assessed the reliability of inferring the features of activation bump lattices according to the measurements of firing fields. First, we reasoned that the association between M_R and C_E was non-accidental. For comparison, we generated 10,000 sets of four pairs of lengths and angles; they were all random numbers, uniformly distributed in the ranges of 40–120 cm and 0° – 30° , respectively, which were numerically comparable with empirical data (Krupic et al., 2015; Stensola et al., 2012). We obtained the resultant estimate for each dataset using the same method as before, and used r_E to gauge the consistency in estimation in terms of both the spacing ratios and orientation differences. The closer r_E was to 2, the more accurate the estimation was (see transparent methods). $\sqrt{r_E}$ was 6.63 ± 1.89 for the real experimental data, whereas it was 9.44 ± 3.39 for the artificial data (Figure 5A); thus, the estimations from the experimental data were much more coherent ($p < 0.05$, two-sample t test). Such comparison indeed highlights the intrinsic correlation between the estimates and experimental data, confirming the feasibility of the estimation method.

Second, we quantified the reliability of estimation. Grid modules M_R actually conferred by combination C_R may be incorrectly estimated to be dictated by combination C_n , i.e., $C_E = C_n \neq C_R$, owing to noise in measurement and combinatorial degeneracy. This noise originated from errors in recording grid spacing and orientation due to limited numbers of grid cells per animal and in module identification (Stensola et al., 2012). Degeneracy refers to that diverse combinations of four modules share the spacing ratios and orientation differences (transparent methods). Thus, one method to evaluate the estimation was to calculate the probability of $C_R = C_m$ under the condition of $C_E = C_n$, i.e., $P(C_R = C_m | C_E = C_n)$; $P(C_R = C_n | C_E = C_n)$ reflects the reliability of estimation. Figure 5B shows 10 leading conditional probabilities based on the

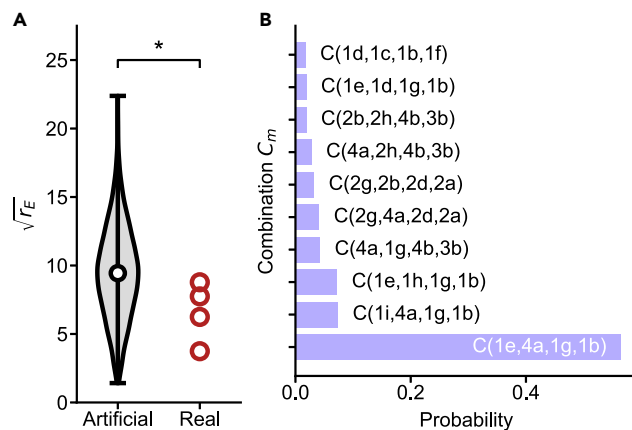


Figure 5. Reliability of estimation

(A) Comparison of $\sqrt{r_E}$ between real and artificial datasets. r_E reflects the extent of consistency between the grid spacing and orientations and estimates. The gray violin plot shows the distribution of $\sqrt{r_E}$ for 10,000 sets of artificial data. The black circle marks the mean value and two bars separately mark the minimum and maximum of $\sqrt{r_E}$. Red circles show $\sqrt{r_E}$ for the data from four rats. * $p < 0.05$, two-sample t test.

(B) Conditional probabilities for 10 combinations given the estimate $C_{E1} = C(1e,4a,1g,1b)$ for rat 1. $P(C_R = C_{E1} | C_E = C_{E1})$ is far greater than the others, indicating the reliability of our estimation.

See also [Figure S6](#).

data from rat 1, and $P(C_R = C_{E1} | C_E = C_{E1})$ was 0.565. The results for rats 2–4 are presented in [Figures S6A–S6C](#). All the previously estimated C_E for each rat had the highest probability, overwhelming any other combination. This justified our estimation and confirmed the conclusions drawn.

Last, although there was no technical difficulty in applying the estimation method to data from rats with only two modules recorded, the estimation would be unreliable for two reasons. First, combinations of two modules were heavily degenerate, which could result in several undistinguishable estimates simultaneously ([Figure S6D](#)). Second, even if two pairs of grid spacing and orientation were randomly chosen, it was still possible to identify a combination with perfect correspondence ([Figure S6E](#)). In fact, $\sqrt{r_E}$ was 3.00 ± 1.05 for random data sets, comparable to that for the empirical data, 3.02 ± 0.19 ; this made such estimation meaningless ([Stensola et al., 2012](#)). Thus, to correctly infer the features of bump attractor lattices from the data on grid spacing and orientation, information about four grid modules per animal may be required.

DISCUSSION

The present work was built on the CAN model. In CAN models, pyramidal cells discharge synchronously to different extents when the activation bump lattice fully or partially matches the pyramidal patch lattice, and 22 such cases are identified. Provided the bump attractor lattice in each module originates from the 22 scenarios, the grid spacing and orientation for each module can be reproduced. This study provides insight into the modularity of grid cells.

Our detailed analyses reveal fine structures in grid spacing and orientation. The spacing ratios between successive modules are predicted to be 1.32–1.59, and the distribution of orientation differences exhibits two peaks around 30° and 0° , as well as some intermediate values. Further, the spacing ratios (S_2/S_1 , S_3/S_2 , and S_4/S_3) can take distinct values for individual animals and exhibit variability between animals. Although rats and mice have different numbers of pyramidal patches and cells per patch ([Naumann et al., 2016](#)), they show a similar distribution of bump spacing normalized by the scale of the pyramidal patch lattice ([Gu et al., 2018](#)). Moreover, it was speculated that there could be up to 10 modules from dorsal to ventral mEC-L2 ([Stensola et al., 2012](#)), whereas our work suggests that the number could be 6.

Previous studies have explored the discretization of spacing ratio from various aspects. In terms of scale relationship across modules, the spacing ratio of $\sqrt{2}$ implies a doubling of the area of a grid hexagon ([Stensola et al., 2012](#)), but the underlying mechanism for the scalar progression and its implications are still obscure. From the perspective of spatial encoding, grid modularity allows for precise position estimation

in a broad environment when the spacing ratio is maintained at 1.5, and the grid orientations were predicted to be identical for different modules (Stemmler et al., 2015). Discretized grid spacing could also be attained via self-organization within a local or global network, while the predicted spacing ratios were less than 1.4 in the local network and too many neurons were required in the global network (Kang and Balasubramanian, 2019; Urdapilleta et al., 2017). Notably, these studies mostly assumed large numbers of grid cells with uniformly distributed grid phases, which actually correspond to stellate cells in our model. Here, we present a different mechanism depending on the geometry of hexagonal lattices. We found that the hexagonal lattice of pyramidal patches endows each module with a specific hexagonal lattice of activity bumps, which further shapes the hexagonal lattice of firing fields. Our work sheds light on the grid modularity besides the mean values of spacing ratios and orientation differences and unravels the modular organizations in four rats within a unifying framework.

The current work not only recapitulates the empirical data on grid spacing and orientation (Figure 4), but also makes the following testable predictions. First, strong synchrony should exist among pyramidal cells rather than stellate cells. Moreover, pyramidal cells from the same module have similar grid phases, or they are divided into subgroups sharing the phase. This is consistent with the report that pyramidal cells in mEC-L2 are phase locked to the theta rhythm of the local field potential and discharge around the same phase (Ray et al., 2014). Second, given the alignment of bump attractors to the patch lattice is intrinsically determined, those quantitative relationships between modules such as spacing ratios and orientation differences should remain the same in different environments. This agrees with the argument that the low-dimensional representation from grid cells is repeatedly used across environments (Fyhn et al., 2007). Third, given the important role for the pyramidal patch lattice, grid modularization and spatial navigation could be interfered with if the activity of pyramidal cells were persistently suppressed. With increasing the duration or degree of pyramidal cell suppression, the modular scale relationships might gradually disintegrate before the grid representation fully disappears. The breakdown of modular scale relationships may not occur before the suppression of stellate cells fully abolishes the bump attractors.

We made three key assumptions in this work. First, each module is organized as a topographic map in mEC, which was suggested by early experiments (Hafting et al., 2005; Heys et al., 2014) and is natural in CAN models (Burak and Fiete, 2009). A recent work provides clear evidence (Gu et al., 2018). Second, pyramidal and stellate cells are connected to constitute a CAN. Although this has not been confirmed directly, accumulating evidence indicates that those pyramidal cells classified as grid cells are located at the edge of patches, closer to stellate cells than other pyramidal cells, and that their firing rates and dynamic features are also similar to those of stellate grid cells (Gu et al., 2018; Ray et al., 2014). Third, bump attractors in different modules maintain the same response to the animal's movement, or equivalently, the grid spacing is proportional to the bump spacing for an animal. The data from mice running on a linear track support this assumption (Gu et al., 2018), and to further justify it may necessitate collecting data from animals running in the 2D environment and analyzing the data at the individual animal level.

It is noteworthy that several issues remain unresolved. First, we provided an intuitive explanation for MI between the animal's location and firing rates of cells, but how that information is further processed is unclear. It is possible that, given the strong synchrony of pyramidal cells, downstream neurons might serve as coincidence detectors (König et al., 1996) and both spike timing and firing-rate coding could be feasible (Li et al., 2009; Wang et al., 2006). Second, while we assume that the large network comprises four modules with increasing the grid spacing along the dorsal-ventral axis of mEC, the underlying mechanism remains elusive. The increase in grid spacing might result from interactions between modules (Kang and Balasubramanian, 2019; Urdapilleta et al., 2017) or a gradient of increasing inhibition along the dorsal-ventral axis (Beed et al., 2013). Third, the influence of stellate cells on grid formation still remains unclear. Apart from the constraints imposed by the pyramidal patch lattice, other mechanisms should be at play to determine specific grid patterns in individual animals. Whether stellate cells play a role in this regard is worth probing. Investigation of these issues may provide further insight into how the network architecture and function can be intimately correlated.

In summary, the current work suggests that the pyramidal patch lattice may be a geometrical template for evoking neuronal activation patterns. This study is the first to unravel how the pyramidal patch lattice guides the discreteness in grid spacing and orientation. Our approach integrating the anatomical architecture and firing dynamics proves useful in figuring out the modularity of grid maps.

Limitations of the study

Our model was built on the empirical data on topographical organization of grid cells (Gu et al., 2018), which were collected only when rats ran on a linear track. The lack of experimental data from animals tested in more situations, such as 2D environments or open fields, suggests that the conclusion of topographical map in the mEC awaits further experimental validation.

Resource availability

Lead contact

Further information and requests for resources should be directed to and will be fulfilled by the lead contact, Feng Liu (fliu@nju.edu.cn).

Materials availability

This study did not generate new unique reagents.

Data and code availability

All data needed to evaluate the conclusions in the paper are present in the paper and [supplemental information](#). Custom python codes will be available upon request to the lead contact.

METHODS

All methods can be found in the accompanying [transparent methods supplemental file](#).

SUPPLEMENTAL INFORMATION

Supplemental information can be found online at <https://doi.org/10.1016/j.isci.2021.102301>.

ACKNOWLEDGMENTS

This work was supported by the National Natural Science Foundation of China (grants 81720108022, 91649116 and 81571040). The numerical calculations in this paper have been performed on the computing facilities at the High Performance Computing Center (HPCC) of Nanjing University.

AUTHOR CONTRIBUTIONS

F.L., T.W., B.Z., and W.W. designed research; T.W. performed research; all authors analyzed the data; T.W. and F.L. wrote the manuscript.

DECLARATION OF INTERESTS

The authors declare no competing interests.

Received: August 30, 2020

Revised: November 15, 2020

Accepted: March 10, 2021

Published: April 23, 2021

REFERENCES

- Beed, P., Bendels, M.H.K., Wiegand, H.F., Leibold, C., Johanning, F.W., and Schmitz, D. (2010). Analysis of excitatory microcircuitry in the medial entorhinal cortex reveals cell-type-specific differences. *Neuron* 68, 1059–1066.
- Beed, P., Gundlfinger, A., Schneiderbauer, S., Song, J., Böhm, C., Burgalossi, A., Brecht, M., Vida, I., and Schmitz, D. (2013). Inhibitory gradient along the dorsoventral axis in the medial entorhinal cortex. *Neuron* 79, 1197–1207.
- Bellmund, J.L.S., Gärdenfors, P., Moser, E.I., and Doeller, C.F. (2018). Navigating cognition: spatial codes for human thinking. *Science* 362, eaat6766.
- Boccaro, C.N., Sargolini, F., Thoresen, V.H., Solstad, T., Witter, M.P., Moser, E.I., and Moser, M.-B. (2010). Grid cells in pre- and parasubiculum. *Nat. Neurosci.* 13, 987–994.
- Bonnevie, T., Dunn, B., Fyhn, M., Hafting, T., Derdikman, D., Kubit, J.L., Roudi, Y., Moser, E.I., and Moser, M.-B. (2013). Grid cells require excitatory drive from the hippocampus. *Nat. Neurosci.* 16, 309–317.
- Brecht, M., Ray, S., Burgalossi, A., Tang, Q., Schmidt, H., and Naumann, R. (2014). An isomorphic mapping hypothesis of the grid representation. *Phil. Trans. R. Soc. B* 369, 20120521.
- Burak, Y., and Fiete, I.R. (2009). Accurate path integration in continuous attractor network models of grid cells. *PLoS Comput. Biol.* 5, e1000291.
- Barry, C., Hayman, R., Burgess, N., and Jeffery, K.J. (2007). Experience-dependent rescaling of entorhinal grids. *Nat. Neurosci.* 10, 682–684.
- Compte, A., Brunel, N., Goldman-Rakic, P.S., and Wang, X.-J. (2000). Synaptic mechanisms and network dynamics underlying spatial working memory in a cortical network model. *Cereb. Cortex* 10, 910–923.
- Constantinescu, A.O., O'Reilly, J.X., and Behrens, T.E.J. (2016). Organizing conceptual knowledge

- in humans with a gridlike code. *Science* 352, 1464–1468.
- Couey, J.J., Witoelar, A., Zhang, S.-J., Zheng, K., Ye, J., Dunn, B., Czajkowski, R., Moser, M.-B., Moser, E.I., Roudi, Y., and Witter, M. (2013). Recurrent inhibitory circuitry as a mechanism for grid formation. *Nat. Neurosci.* 16, 318–324.
- Dawitz, J., Kroon, T., Hjorth, J.J.J., Mansvelde, H.D., and Meredith, R.M. (2020). Distinct synchronous network activity during the second postnatal week of medial entorhinal cortex development. *Front. Cell. Neurosci.* 14, 91.
- Doeller, C.F., Barry, C., and Burgess, N. (2010). Evidence for grid cells in a human memory network. *Nature* 463, 657–661.
- Domnisoru, C., Kinkhabwala, A.A., and Tank, D.W. (2013). Membrane potential dynamics of grid cells. *Nature* 495, 199–204.
- Epstein, R.A., Patai, E.Z., Julian, J.B., and Spiers, H.J. (2017). The cognitive map in humans: spatial navigation and beyond. *Nat. Neurosci.* 20, 1504–1513.
- Fuchs, E.C., Neitz, A., Pinna, R., Melzer, S., Caputi, A., and Monyer, H. (2016). Local and distant input controlling excitation in layer II of the medial entorhinal cortex. *Neuron* 89, 194–208.
- Fuhs, M.C., and Touretzky, D.S. (2006). A spin glass model of path integration in rat medial entorhinal cortex. *J. Neurosci.* 26, 4266–4276.
- Fyhn, M., Hafting, T., Treves, A., Moser, M.-B., and Moser, E.I. (2007). Hippocampal remapping and grid realignment in entorhinal cortex. *Nature* 446, 190–194.
- Fyhn, M., Hafting, T., Witter, M.P., Moser, E.I., and Moser, M.-B. (2008). Grid cells in mice. *Hippocampus* 18, 1230–1238.
- Gu, Y., Lewallen, S., Kinkhabwala, A.A., Domnisoru, C., Yoon, K., Gauthier, J.L., Fiete, I.R., and Tank, D.W. (2018). A map-like micro-organization of grid cells in the medial entorhinal cortex. *Cell* 175, 736–750.
- Hafting, T., Fyhn, M., Molden, S., Moser, M.-B., and Moser, E.I. (2005). Microstructure of a spatial map in the entorhinal cortex. *Nature* 436, 801–806.
- Heys, J.G., Rangarajan, K.V., and Dombeck, D.A. (2014). The functional micro-organization of grid cells revealed by cellular-resolution imaging. *Neuron* 84, 1079–1090.
- Jacobs, J., Weidemann, C.T., Miller, J.F., Solway, A., Burke, J.F., Wei, X.-X., Suthana, N., Sperling, M.R., Sharan, A.D., Fried, I., and Kahana, M.J. (2013). Direct recordings of grid-like neuronal activity in human spatial navigation. *Nat. Neurosci.* 16, 1188–1190.
- König, P., Engel, A.K., and Singer, W. (1996). Integrator or coincidence detector? The role of the cortical neuron revisited. *Trends Neurosci.* 19, 130–137.
- Kang, L., and Balasubramanian, V. (2019). A geometric attractor mechanism for self-organization of entorhinal grid modules. *eLife* 8, e46687.
- Killian, N.J., Jutras, M.J., and Buffalo, E.A. (2012). A map of visual space in the primate entorhinal cortex. *Nature* 491, 761–764.
- Kitamura, T., Pignatelli, M., Suh, J., Kohara, K., Yoshiki, A., Abe, K., and Tonegawa, S. (2014). Island cells control temporal association memory. *Science* 343, 896–901.
- Koenig, J., Linder, A.N., Leutgeb, J.K., and Leutgeb, S. (2011). The spatial periodicity of grid cells is not sustained during reduced theta oscillations. *Science* 332, 592–595.
- Krupic, J., Bauza, M., Burton, S., Barry, C., and O’Keefe, J. (2015). Grid cell symmetry is shaped by environmental geometry. *Nature* 518, 232–235.
- Li, J., Liu, F., Xu, D., and Wang, W. (2009). Signal propagation through feedforward neuronal networks with different operational modes. *EPL* 85, 38006.
- Naumann, R.K., Ray, S., Prokop, S., Las, L., Heppner, F.L., and Brecht, M. (2016). Conserved size and periodicity of pyramidal patches in layer 2 of medial/caudal entorhinal cortex. *J. Comp. Neurol.* 524, 783–806.
- O’Neill, J., Boccara, C.N., Stella, F., Schoenenberger, P., and Csicsvari, J. (2017). Superficial layers of the medial entorhinal cortex replay independently of the hippocampus. *Science* 355, 184–188.
- Park, S.A., Miller, D.S., Nili, H., Ranganath, C., and Boorman, E.D. (2020). Map making: Constructing, combining, and inferring on abstract cognitive maps. *Neuron* 107, 1226–1238.
- Ray, S., Burgalossi, A., Brecht, M., and Naumann, R.K. (2017). Complementary modular microcircuits of the rat medial entorhinal cortex. *Front. Syst. Neurosci.* 11, 20.
- Ray, S., Naumann, R., Burgalossi, A., Tang, Q., Schmidt, H., and Brecht, M. (2014). Grid-layout and theta-modulation of layer 2 pyramidal neurons in medial entorhinal cortex. *Science* 343, 891–896.
- Rowland, D.C., Obenhaus, H.A., Skytøen, E.R., Zhang, Q., Kentros, C.G., Moser, E.I., and Moser, M.-B. (2018). Functional properties of stellate cells in medial entorhinal cortex layer II. *eLife* 7, e36664.
- Rowland, D.C., Roudi, Y., Moser, M.-B., and Moser, E.I. (2016). Ten years of grid cells. *Annu. Rev. Neurosci.* 39, 19–40.
- Stemmler, M., Mathis, A., and Herz, A.V.M. (2015). Connecting multiple spatial scales to decode the population activity of grid cells. *Sci. Adv.* 1, e1500816.
- Stensola, H., Stensola, T., Solstad, T., Frøland, K., Moser, M.-B., and Moser, E.I. (2012). The entorhinal grid map is discretized. *Nature* 492, 72–78.
- Stensola, T., Stensola, H., Moser, M.-B., and Moser, E.I. (2015). Shearing-induced asymmetry in entorhinal grid cells. *Nature* 518, 207–212.
- Sun, C., Kitamura, T., Yamamoto, J., Martin, J., Pignatelli, M., Kitch, L.J., Schnitzer, M.J., and Tonegawa, S. (2015). Distinct speed dependence of entorhinal island and ocean cells, including respective grid cells. *Proc. Natl. Acad. Sci. U S A* 112, 9466–9471.
- Tang, Q., Burgalossi, A., Ebbesen, C.L., Sanguinetti-Scheck, J.I., Schmidt, H., Tukker, J.J., Naumann, R., Ray, S., Preston-Ferrer, P., Schmitz, D., and Brecht, M. (2016). Functional architecture of the rat parasubiculum. *J. Neurosci.* 36, 2289–2301.
- Unichenko, P., Yang, J.-W., Luhmann, H.J., and Kirischuk, S. (2015). Glutamatergic system controls synchronization of spontaneous neuronal activity in the murine neonatal entorhinal cortex. *Pflügers Arch.* 467, 1565–1575.
- Urdapilleta, E., Si, B., and Treves, A. (2017). Selforganization of modular activity of grid cells. *Hippocampus* 27, 1204–1213.
- Varga, C., Lee, S.Y., and Soltesz, I. (2010). Target-selective GABAergic control of entorhinal cortex output. *Nat. Neurosci.* 13, 822–824.
- Wang, S., Wang, W., and Liu, F. (2006). Propagation of firing rate in a feed-forward neuronal network. *Phys. Rev. Lett.* 96, 018103.
- Xue, C., and Liu, F. (2014). Structured synaptic inhibition has a critical role in multiple-choice motion-discrimination tasks. *J. Neurosci.* 34, 13444–13457.
- Yartsev, M.M., Witter, M.P., and Ulanovsky, N. (2011). Grid cells without theta oscillations in the entorhinal cortex of bats. *Nature* 479, 103–107.
- Zutshi, I., Fu, M.L., Lilascharoen, V., Leutgeb, J.K., Lim, B.K., and Leutgeb, S. (2018). Recurrent circuits within medial entorhinal cortex superficial layers support grid cell firing. *Nat. Commun.* 9, 3701.

iScience, Volume 24

Supplemental information

**Modularization of grid cells constrained
by the pyramidal patch lattice**

Tao Wang, Fan Yang, Ziqun Wang, Bing Zhang, Wei Wang, and Feng Liu

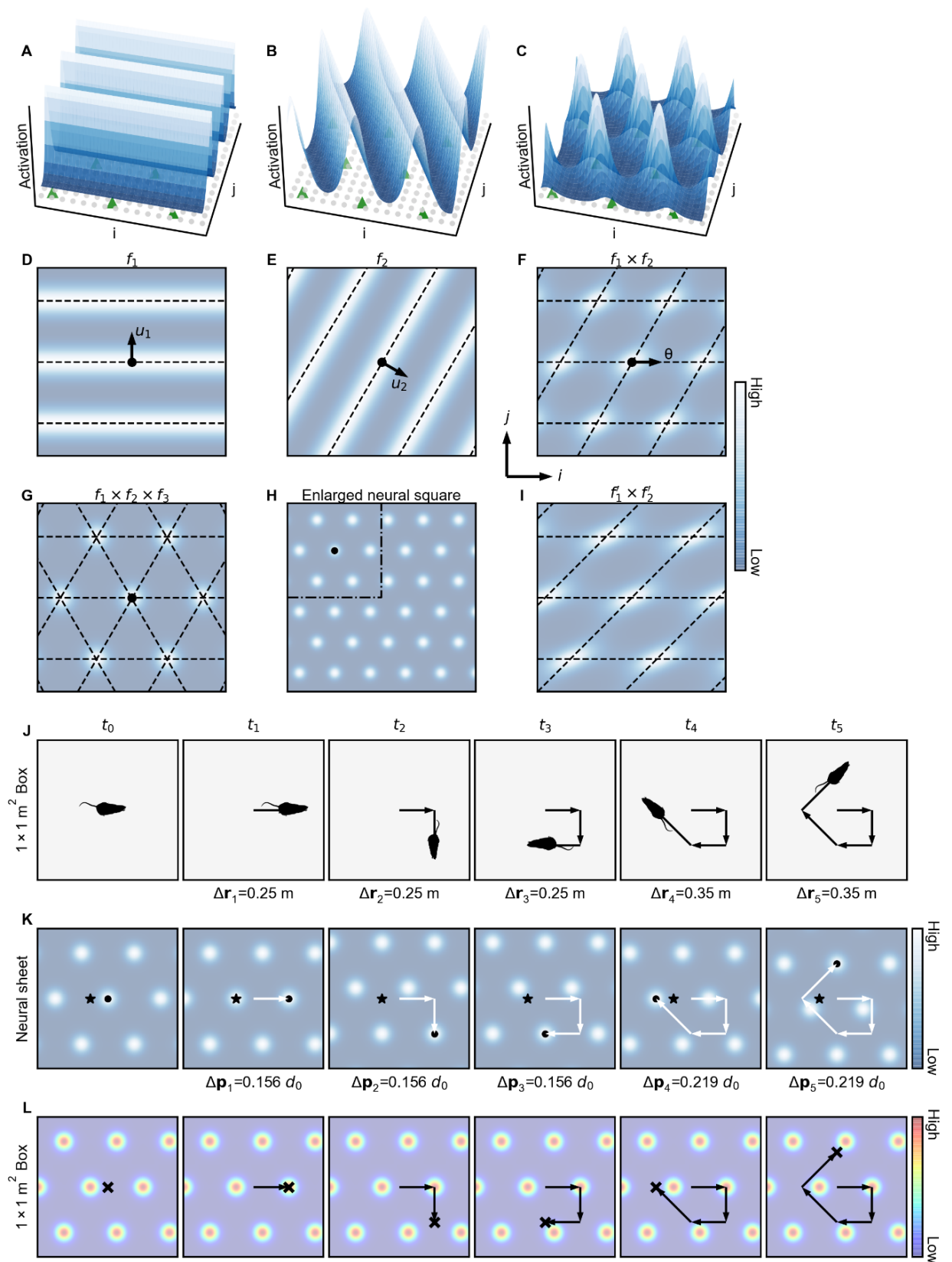


Figure S1. Emergence of hexagonally distributed activation bumps and firing fields (related to Figure 1).

(A and B) Surface plots of two one-dimensional (1D) von Mises function $f_1(i, j)$ with $\mathbf{u}_1 = (0, 1)$ (A) and $f_2(i, j)$ with $\mathbf{u}_2 = (\sqrt{3}/2, -1/2)$ (B). The green triangles and gray dots at the bottom represent pyramidal patches and stellate cells, respectively, and their activation states are marked in z -axis.

(C) Surface plot of the product of $f_1(i, j)$ and $f_2(i, j)$. The activation bumps are hexagonally distributed because of specific choices of \mathbf{u}_1 and \mathbf{u}_2 .

(D and E) Heat map of $f_1(i, j)$ (D) and $f_2(i, j)$ (E). The black arrow denotes the direction of \mathbf{u}_1 and \mathbf{u}_2 , while dashed lines mark the zero phases. As $f_1(i, j)$ and $f_2(i, j)$ involve the cosine function, zero phase corresponds to the highest firing rate.

(F) Heat map of the product of $f_1(i, j)$ and $f_2(i, j)$. Bumps are centered at cross points of zero phase lines of $f_1(i, j)$ and $f_2(i, j)$, representing the points with the highest firing rate. Notably, the bumps are in the shape of ellipse because only two directions are considered.

(G) Heat map of the product of $f_1(i, j)$, $f_2(i, j)$ and $f_3(i, j)$. The bumps are of perfect circular shape.

(H) A larger neural square with quadruple areas. The other parameters are the same as in (G), and the enclosed area by dash-dotted lines corresponds to that in (G).

(I) Heat map of the product of $f'_1(i, j)$ and $f'_2(i, j)$ with $\mathbf{u}'_1 = (0, 1)$ and $\mathbf{u}'_2 = (\sqrt{2}/2, -\sqrt{2}/2)$. The bumps are not hexagonally distributed in this case.

(J) The animal's movement in a $1 \times 1 \text{ m}^2$ box at t_0 - t_5 . The black arrows denote the animal's path, and the distance between t_{i-1} and t_i is marked with $\Delta \mathbf{r}_i$.

(K) Snapshots of the neural sheet corresponding to J. The firing rate at each point is represented in blue scale. Pyramidal and stellate cells are not distinguished here. The center of a bump is indicated by black dot, and its shift by white arrow.

(L) Firing fields of the star-labeled neuron in (K). The firing activity is color coded. The black cross marks the animal's location, and the black arrow indicates the animal's movement. Panels (J-L) exemplify how the activation bumps and the animal's movement are correlated.

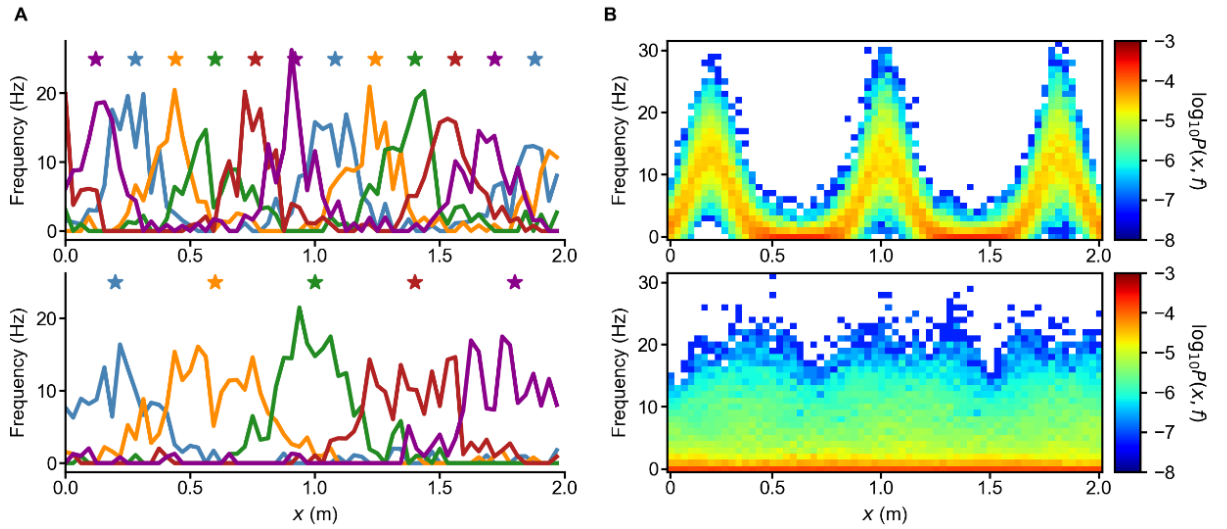


Figure S2. Firing rates of stellate cells and the joint probability between the animal's position and firing rates of pyramidal cells, $P(\mathbf{r}, f)$ (related to Figure 2).

(A) Shown are the firing rates of five stellate cells versus the position along the dashed line in Figure 2C on a trial. The center of firing field is marked by star. Stellate cells are equidistantly selected along the x -axis with a distance of $0.25d_0$ and $0.1d_0$, respectively, for the upper and lower panels.

(B) $P(\mathbf{r}, f)$ was estimated from 3900 firing fields (39 pyramidal cells and 100 trials per cell). $P(\mathbf{r}, f)$ is a 3D matrix, and its slice over the x -axis is shown. The upper and lower panels correspond to the cases of synchronous and asynchronous firing, respectively, in Figure 2.

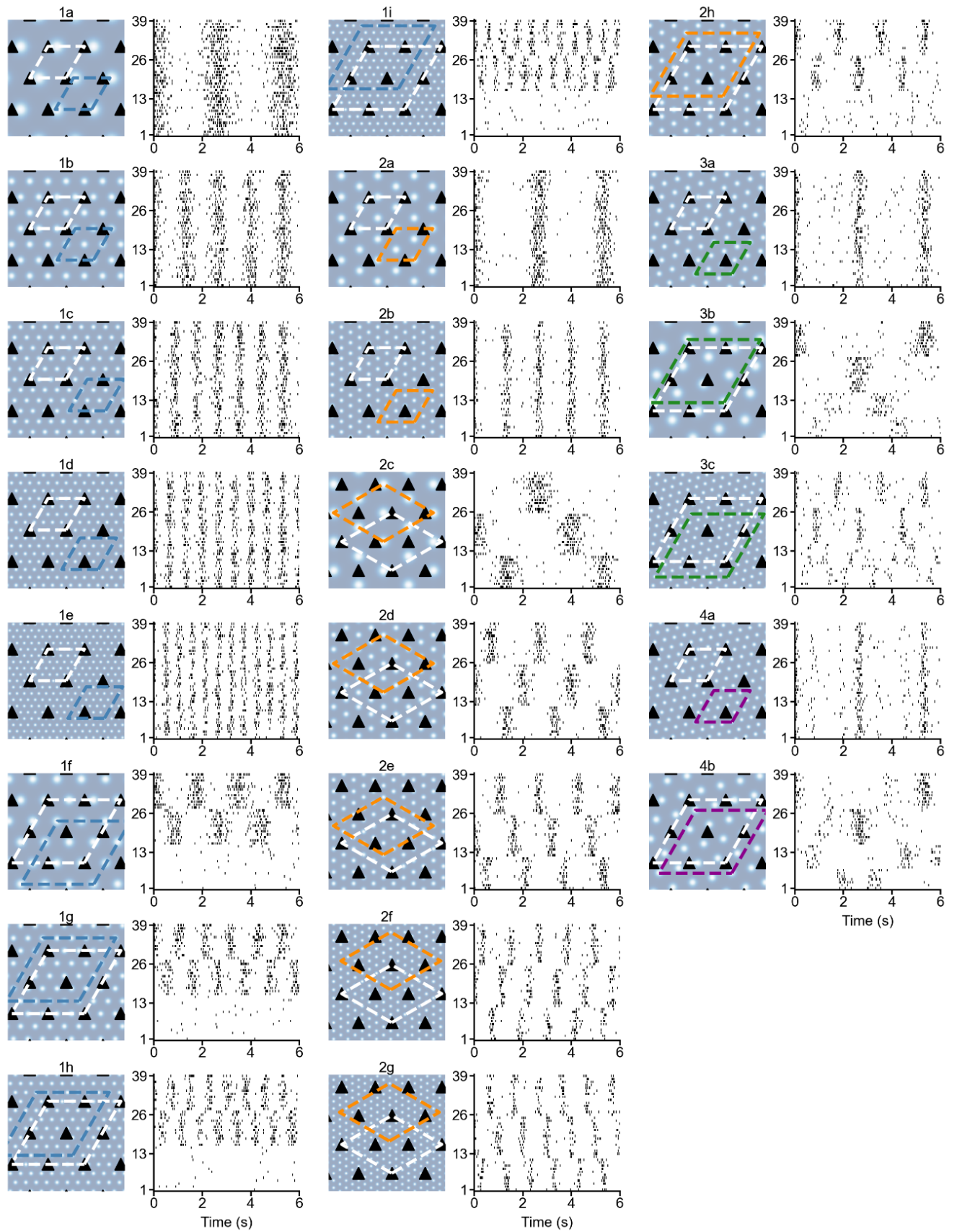


Figure S3. Geometrical and spiking features of all 22 cases (related to Figure 3).

The left column of each case shows the relationship between the activation pattern and the pyramidal patch lattice. Displayed are matching units of the activation pattern (colored rhombus) and the patch lattice (white rhombus). **The right column** of each case shows the spatiotemporal firing pattern of pyramidal cells. Neurons are sorted according to their synchrony in each panel. The ordinate and abscissa are the neural label and time, respectively.

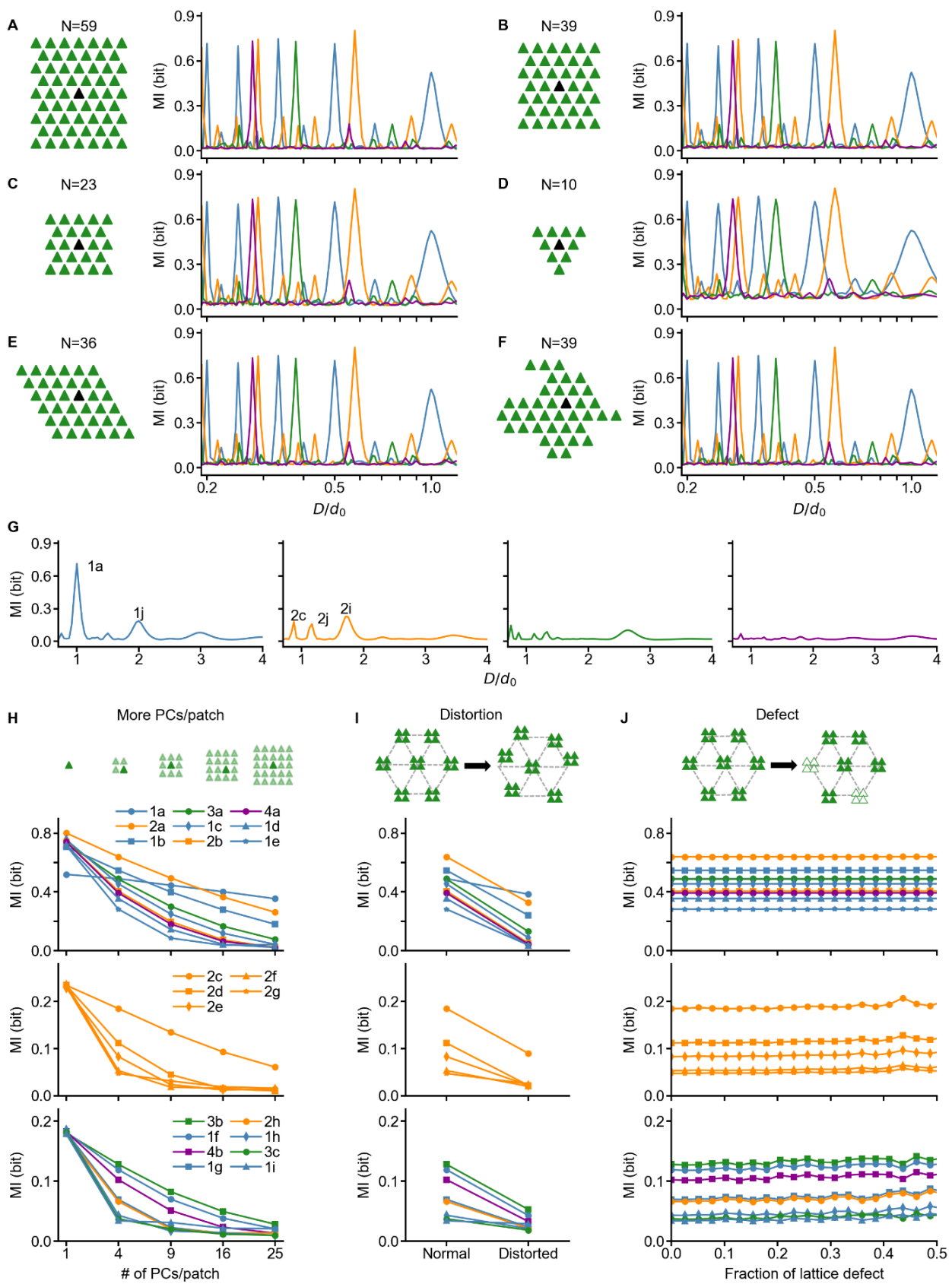


Figure S4. Robustness of MI peaks under complex conditions (related to Figure 3).

(A-F) Results for six situations of the pyramidal patch lattice with different scales and shapes. The left column displays the schematic, where each triangle labels a pyramidal patch, and stellate cells are hidden for simplicity. The number of pyramidal patches is marked on the top. The black triangle is the initial position of a bump attractor's center, i.e., $\mathbf{p}_{\text{Max}}(t = 0)$. The right column shows the corresponding MI curves, where four colors represent four distinct orientations as in Figure 3. 22 MI peaks are robustly present in each case.

(G) Curves of the MI versus D with $D > d_0$ for different orientations. Only one secondary peak (2i) and two tertiary peaks (1j and 2j) appear. Here, $\alpha = 2.67$ was set to ensure the scale of firing fields in a reasonable range relative to the $2 \times 2 \text{ m}^2$ box.

(H) Results for the cases with more pyramidal cells per patch in an ideal lattice. The MI peak height drops with increasing the number of pyramidal cells per patch. Top plots show the structure of individual patches comprising 1, 4, 9, 16 and 25 pyramidal cells. The second, third, fourth rows show the results for the cases with a primary, secondary, or tertiary MI peak in Figure 3C, respectively (here and thereafter).

(I) Comparison of peak heights between the cases with normal and distorted lattices. Each patch comprised four cells. In the distortion case the MI was averaged over 10 independent simulations, where the lattice was distorted differently.

(J) The peak height versus the fraction of defect vertexes. Each patch comprised four cells. The MI was calculated by averaging over 10 independent simulations, where different vertexes got lost. In all cases, apart from the scale and shape of the lattice, details of each patch and the specified modification, other parameters remained the same.

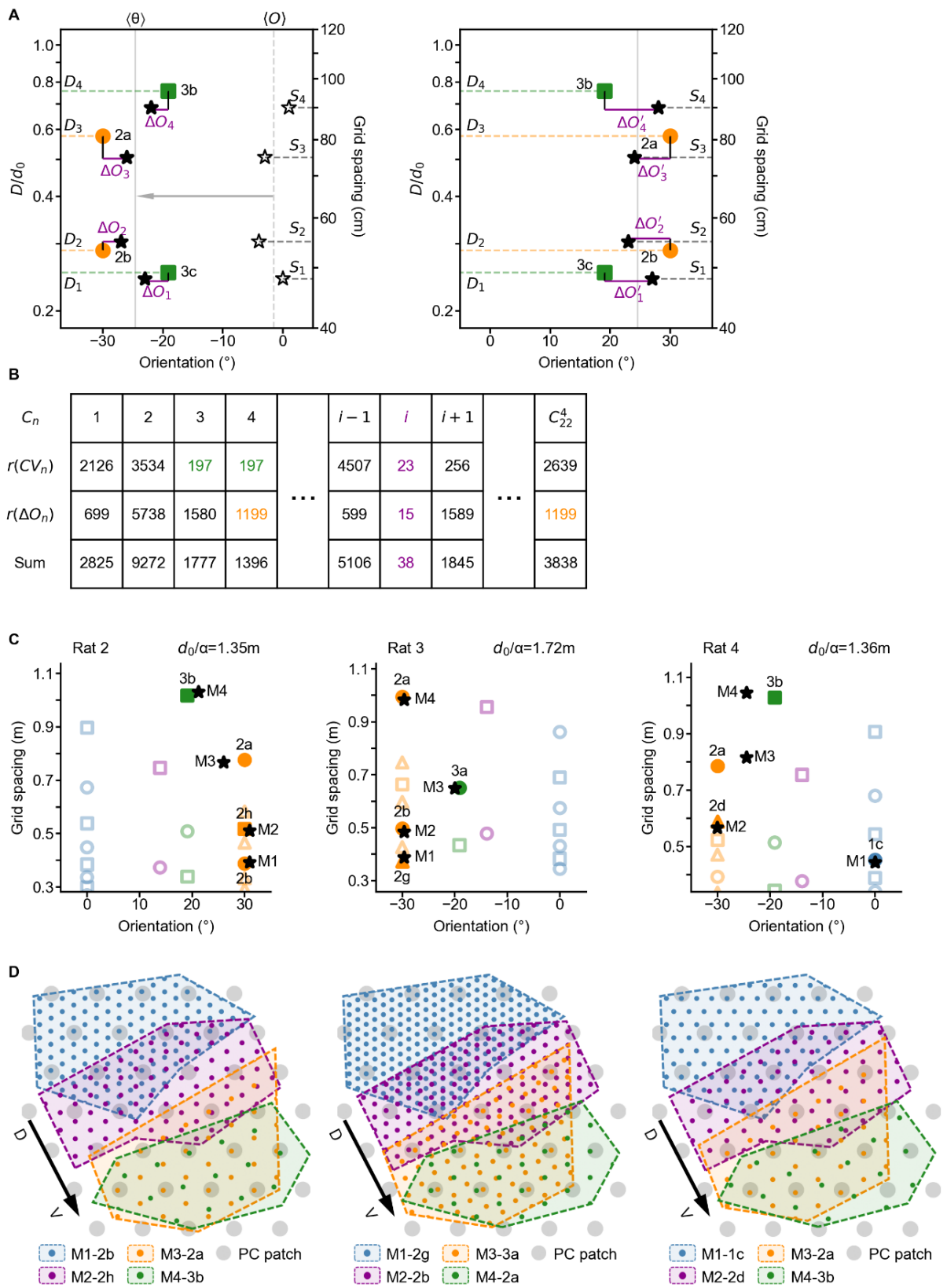


Figure S5. Estimation of the grid spacing and orientation (related to Figure 4).

(A) Schematic of calculating the $CV(M_R, C_n)$ and $\Delta O(M_R, C_n)$. The left and right panels separately illustrate the normal and inverse manner of correspondence. Four colored solid symbols label a combination C_n , and the corresponding bump spacing D_i is marked on the left axis. Four hollow stars label the experimental recording of grid modules, M_R , and the corresponding grid spacing S_i is marked on the right axis. The solid and dashed gray lines indicate the mean orientation of C_n and M_R , respectively. The solid stars denote M_R after the redefinition of zero-orientation of the environment. Thus, the four ΔO_i 's are illustrated in purple, and S_i/D_i can be easily obtained. In the right panel, the original experimental recordings are not shown.

(B) The rank method for determining C_E . $CV(M_R, C_n)$ and $\Delta O(M_R, C_n)$ were separately ranked in an ascending order. Given $CV(M_R, C_3) = CV(M_R, C_4)$, they were assigned the same rank 197 (green), and the next number 198 was skipped. It was similarly done with $\Delta O(M_R, C_n)$ (yellow). The combination with the minimum r_E (purple column) was selected as the estimate C_E .

(C) Relationship between the grid spacing and orientation for the three rats in Stensola *et al.* 2012. Shown are the experimental data (black stars) and the estimates (solid symbols). Open symbols represent the results for other cases featuring a primary (circle), secondary (triangle) or tertiary (square) MI peak.

(D) Schematic of modularization of grid cells in mEC-L2 for the three rats in (Stensola *et al.*, 2012). Different colors label distinct modules. The shadow, dots, and circles represent grid cells, activation bumps, and pyramidal patches, respectively. The boundary of each module is arbitrary.

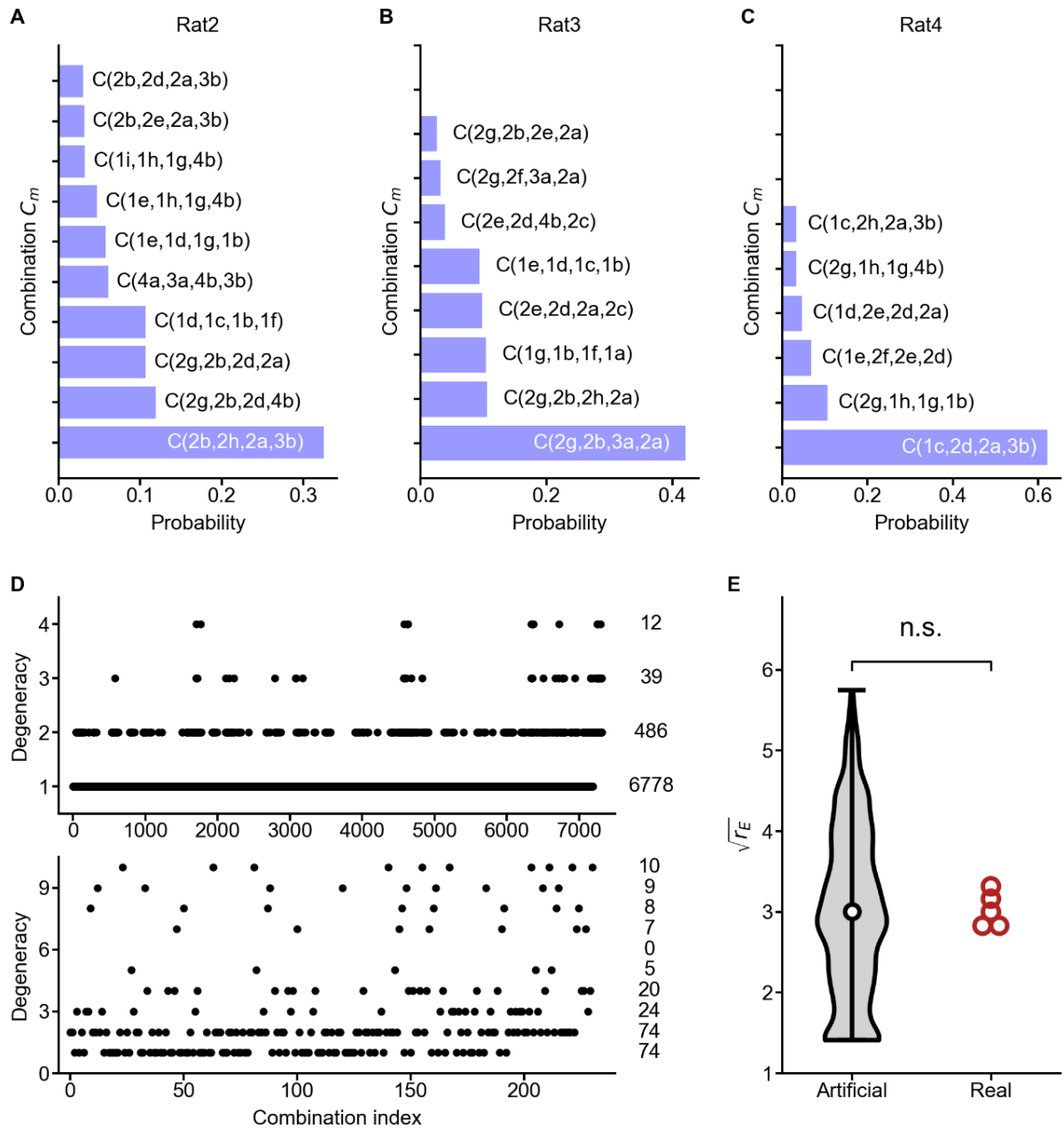


Figure S6. Reliability of estimation (related to Figure 5).

(A-C) Conditional probabilities when the estimated combinations were $C_{E2} = C(2b, 2h, 2a, 3b)$, $C_{E3} = C(2g, 2b, 3a, 2a)$, and $C_{E4} = C(1c, 2d, 2a, 3b)$, respectively, for Rats 2-4 in Stensola *et al.*, 2012. For each rat, the probability of the estimate, $P(C_R = C_{Ei} | C_E = C_{Ei})$, predominates.

(D) Degeneracy for combinations of four (top) and two (bottom) modules, respectively. Numbers to the right denote the total number of combinations with that degeneracy.

(E) Comparison of $\sqrt{r_E}$ between the empirical and artificial data sets. The grey violin plot shows the distribution of $\sqrt{r_E}$ for 10000 sets of two artificial pairs of spacing and orientation. Red circles show $\sqrt{r_E}$ for the experimental data on two modules from five rats in Stensola *et al.*, 2012. $P=0.42$, two-sample t -test.

Supplemental Tables

Table S1: Experiments on grid cell modules (related to Figure 4).

Reference	Barry <i>et al.</i> (2007)	Stensola <i>et al.</i> (2012)	Krupic <i>et al.</i> (2015)	Gu <i>et al.</i> (2018)
# of animals	6 rats	15 rats	11 rats	6 mice
# of module pairs recorded	6	24	11	10
Mean spacing ratio	1.7	1.42	1.56	1.51
Orientation data available	No	Yes	Yes	No

Table S2: Experimental data from Stensola *et al.* (2012) (related to Figure 4).

Rat 1		Rat 2		Rat 3		Rat 4	
S (cm)	O (°)						
46.6	-0.43	39.2	4.44	38.8	-3.97	44.4	14.9
63.9	6.21	51.2	4.44	48.4	-3.97	56.7	-15.1
93.4	-2.81	76.8	-0.51	65.0	5.69	81.7	-9.6
118.9	-3.49	103.1	-5.30	98.4	-3.97	104.5	-9.6

Table S3: Vertexes of the pyramidal patch lattice in a module (related to Figure 1).

Patch	Location (<i>i, j</i>)						
1	(-2.5,-2.60)	11	(2,-1.73)	21	(1,0)	31	(0,1.73)
2	(-1.5,-2.60)	12	(-2.5,-0.87)	22	(2,0)	32	(1,1.73)
3	(-0.5,-2.60)	13	(-1.5,-0.87)	23	(-2.5,0.87)	33	(2,1.73)
4	(0.5,-2.60)	14	(-0.5,-0.87)	24	(-1.5,0.87)	34	(-2.5,2.60)
5	(1.5,-2.60)	15	(0.5,-0.87)	25	(-0.5,0.87)	35	(-1.5,2.60)
6	(2.5,-2.60)	16	(1.5,-0.87)	26	(0.5,0.87)	36	(-0.5,2.60)
7	(-2,-1.73)	17	(2.5,-0.87)	27	(1.5,0.87)	37	(0.5,2.60)
8	(-1,-1.73)	18	(-2,0)	28	(2.5,0.87)	38	(1.5,2.60)
9	(0,-1.73)	19	(-1,0)	29	(-2,1.73)	39	(2.5,2.60)
10	(1,-1.73)	20	(0,0)	30	(-1,1.73)		

Table S4: Default parameter values and initial condition of the model (related to Figures 1-5).

Parameter	Value	Unit
F_m	15	Hz
κ	1.0	
α	1/1.6	$d_0 \text{ m}^{-1}$
Box area	2×2	m^2
Variable	Initial value	Unit
p_{Max}	(0,0)	
r	(1,1)	m

TRANSPARENT METHODS

Simulating the animal's movement in a box

Without experimental data available, we simulated the running path of an animal in a square box of $2 \times 2 \text{ m}^2$ as follows. The animal ran at a speed of $s(t)$ in the direction of $\psi(t)$, and its position $\mathbf{r} = (x, y)$ obeyed the differential equations:

$$\begin{cases} \frac{dx}{dt} = s(t) \cdot \cos(\psi(t)) \\ \frac{dy}{dt} = s(t) \cdot \sin(\psi(t)) \end{cases} \quad (5)$$

where the x -axis was further assumed to parallel one of the box boundaries (the equation numbering here is a continuation of that in the main text). $s(t)$ and $\psi(t)$ slightly changed over each time step, following

$$\begin{cases} s(t + \Delta t) = s(t) + \delta s \\ \psi(t + \Delta t) = \psi(t) + \delta \psi, \end{cases} \quad (6)$$

where δs and $\delta \psi$ were assumed to obey the normal distributions, $\delta s \sim N(0, (\frac{1}{1000})^2)$ and $\delta \psi \sim N(0, (\frac{\pi}{180})^2)$, and the time step $\Delta t = 4 \text{ ms}$. Two factors should be taken into account: the animal cannot run out of the box and thus has to make a turn at the boundary, and the running speed is not high, 0.2-0.8 m/s, according to the experimental protocol (Góis and Tort, 2018; Hinman et al., 2016; Kropff et al., 2015; Sun et al., 2015). Ten virtual paths of 4096 s were generated.

Firing maps of cells on single trials

Firing map of a grid cell characterizes its firing activity on a single trial, different from its firing field obtained via averaging over many trials. With the box of $2 \times 2 \text{ m}^2$ divided into 64×64 bins, the firing rate was defined as the number of spikes in each bin divided by the total time when the animal stayed in this bin. Figure 2D shows one example of firing maps for all 39 pyramidal cells along the x -axis.

Mutual information (MI) between spatial location and firing rate

To calculate the mutual information between the animal's position and firing rates of all pyramidal cells, we performed 100 simulations with 10 different virtual paths and 10 trials per path under the same initial condition, recording the spikes of pyramidal cells. We got 3900 firing maps altogether. The firing rate from 0 to 32 Hz was uniformly divided into 32 bins. The MI between the spatial position (\mathbf{r}) and firing rates of pyramidal cells (f) was given by

$$MI(\mathbf{r}; f) = \sum_{all \mathbf{r}} \sum_{all f} P(\mathbf{r}, f) \cdot \log_2 \left(\frac{P(\mathbf{r}, f)}{P(\mathbf{r})P(f)} \right) \quad (7)$$

where the base-2 logarithm allows the MI to be measured in units of bits. The probabilities $P(\mathbf{r}, f)$, $P(\mathbf{r})$ and $P(f)$ were estimated by conducting statistical analysis of firing maps in each 3D (2D for space and 1D for firing rate), 2D (space) and 1D (firing rate) bin, respectively. A slice of $P(\mathbf{r}, f)$ is shown in Figure S2B.

More pyramidal cells per patch, lattice distortion and defect

Apart from the simplest case of one pyramidal cell per patch, four more situations with a larger patch size were considered, where the number of representative pyramidal cells per patch was 4, 9, 16 and 25, respectively. These patches were modeled by equidistantly adding more cells around the original one with a distance of $0.1d_0$ (Figure S4H). For $d_0 = 300 \mu\text{m}$, the patch comprising 4, 9, 16 or 25 pyramidal cells covered the area of 30×30 , 60×60 , 90×90 , and $120 \times 120 \mu\text{m}^2$, respectively.

In the case of lattice distortion, some patches, comprising four pyramidal cells, randomly deviated from vertexes, with the deviation ranging from $-0.2d_0$ to $0.2d_0$ along the i - and j -axis (Figure S4I). In the case of lattice defect, some patches were discarded randomly (Figure S4J). Each retained patch comprised four pyramidal cells.

Estimating the bump spacing and orientation according to empirical data on grid spacing and orientations

$M_n = \{(S_n^1, O_n^1), (S_n^2, O_n^2), (S_n^3, O_n^3), (S_n^4, O_n^4)\}$ ($S_n^4 > S_n^3 > S_n^2 > S_n^1$) denoted the four grid modules conferred by the combination of four scenarios

$C_n = \{(D_n^1, \theta_n^1), (D_n^2, \theta_n^2), (D_n^3, \theta_n^3), (D_n^4, \theta_n^4)\}$ ($D_n^4 > D_n^3 > D_n^2 > D_n^1$), with $n = 1, 2, \dots, 7315$. According to Eqs. (3) and (4) in the main text, we got

$$\frac{S_n^j}{S_n^i} = \frac{D_n^j}{D_n^i}, \quad \forall i, j = 1 - 4 \quad (8)$$

$$|O_n^j - O_n^i| = |\theta_n^j - \theta_n^i|, \quad \text{and } j > i \quad (9)$$

For another M_m conferred by C_m ($m \neq n$), M_m and C_n usually did not satisfy Eqs. (8) and (9).

Theoretically, we could obtain C_n directly using Eqs. (8) and (9) given M_n . In fact, we did not do that for two reasons. First, there were actually 12 identities following Eqs. (8) and (9), which made the calculation extremely time-consuming. Second, the recorded M_n was always noisy, such that Eqs. (8) and (9) could not strictly hold simultaneously. Thus, we had to transform these two equations. Eq. (8) gave

$$\frac{S_n^i}{D_n^i} = \frac{S_n^j}{D_n^j} = \frac{1}{\alpha_n}, \quad i, j = 1 - 4 \quad (10)$$

For M_m and C_n ($m \neq n$), S_m^i/D_n^i usually took different values from $1/\alpha_n$ for $i=1-4$. Thus, the coefficient of variation of S_m^i/D_n^i , denoted as $CV(M_m, C_n)$, could be used to characterize the spacing relation between M_m and C_n . $CV(M_m, C_n) = 0$ for $m = n$.

Eq. (9) could be transformed into

$$O_n^i - (\pm\theta_n^i) = O_n^j - (\pm\theta_n^j). \quad i, j = 1 - 4 \quad (11)$$

\pm represents the normal and the inverse manner of correspondence between M_n and C_n (see Figure S5A for details), which were mutually exclusive in general. Thus, $O_n^i - (\pm\theta_n^i)$ was identical for $i = 1 - 4$, whereas $O_m^i - (\pm\theta_n^i)$ usually took different values for M_m and C_n ($m \neq n$). Actually, the offsets between O_m^i and $(\pm\theta_n^i)$ largely depended on the definition of zero-orientation of the environment. To eliminate the effect due to distinct definition and further simplify the equation, we considered the grid orientation relative to the mean bump orientation, which was essentially a redefinition of zero-orientation of the environment according to the

bump orientation (Figure S5A):

$$\tilde{O}_n^i = O_n^i + \langle \pm\theta \rangle_n - \langle O \rangle_n, \quad i = 1 - 4 \quad (12)$$

where $\langle \pm\theta \rangle_n = \pm \sum_{i=1}^4 \theta_n^i / 4$ and $\langle O \rangle_n = \sum_{i=1}^4 O_n^i / 4$. Consequently, we had

$$\tilde{O}_n^i - (\pm\theta_n^i) = 0, \quad i = 1 - 4 \quad (13)$$

Thus, $\sum_{i=1}^4 |\tilde{O}_n^i - (\pm\theta_n^i)| = 0$, whereas $\sum_{i=1}^4 |\tilde{O}_m^i - (\pm\theta_n^i)| > 0$ for M_m and C_n ($m \neq n$). $\Delta O(M_m, C_n), \min(\sum_{i=1}^4 |\tilde{O}_m^i - \theta_n^i|, \sum_{i=1}^4 |\tilde{O}_m^i - (-\theta_n^i)|)$, was used to characterize the orientation relation between M_m and C_n . $\Delta O(M_m, C_n) = 0$ for $m = n$.

Ideally, given M_R , the correspondence C_R should satisfy $CV(M_R, C_R) = 0$ and $\Delta O(M_R, C_R) = 0$. In the presence of noise, $CV(M_R, C_R)$ and $\Delta O(M_R, C_R)$ could not be zero generally. If noise was not so large, they should be much smaller than $CV(M_R, C_n)$ and $\Delta O(M_R, C_n)$ ($C_n \neq C_R$), respectively. Thus, a rank method was used to identify an estimate of C_R , denoted as C_E . We calculated $CV(M_R, C_n)$ and $\Delta O(M_R, C_n)$ for all C_n and then ranked them in an ascending order; in this way we got (CV_n) , $r(\Delta O_n)$, and their sum $r_E = r(CV_n) + r(\Delta O_n)$. If $CV(M_R, C_n) = CV(M_R, C_m)$, they were assigned the same rank, $r(CV_n) = r(CV_m) = a$, and the next rank number, $a + 1$, should be skipped, as was done with $\Delta O(M_R, C_n)$. The combination with r_E being the minimum was chosen as the estimate C_E (Figure S5B). Without noise, $r(CV_R) = 1$ and $r(\Delta O_R) = 1$, leading to $r_E = 2$. Thus, r_E reflects the reliability of estimation; the closer r_E was to 2, the more reliable the estimate was.

Degenerate combinations of modules from the 22 scenarios

Apart from the noise, combinational degeneracy was another factor affecting estimation. There were totally $C_{22}^2 = 231$ combinations of two modules and $C_{22}^4 = 7315$ combinations of four modules from all the 22 scenarios. Although each combination had its own set of bump spacing and orientation, these combinations might be undistinguishable in terms of spacing ratio and orientation difference

between modules. For example, two combinations $C(1b, 2c)$ and $C(1c, 2a)$ had the same spacing ratio and orientation difference, i.e. $\frac{D_{2c}}{D_{1b}} = \frac{D_{2a}}{D_{1c}} = \sqrt{3}$ and $|\theta_{2c} - \theta_{1b}| = |\theta_{2a} - \theta_{1c}| = 30^\circ$. Thus, if two grid modules of an animal had the spacing ratio of $\frac{S_2}{S_1} = \sqrt{3}$ and orientation difference of $|O_2 - O_1| = 30^\circ$, it would be unable to determine whether the two grid modules were conferred by $C(1b, 2c)$ or $C(1c, 2a)$ with our rank method. Hence, $C(1b, 2c)$ and $C(1c, 2a)$ were termed degenerate combinations.

Mathematically, two combinations $C(x_1, x_2) = \{(D_{x_1}, \theta_{x_1}), (D_{x_2}, \theta_{x_2})\}$ and $C(y_1, y_2) = \{(D_{y_1}, \theta_{y_1}), (D_{y_2}, \theta_{y_2})\}$ were degenerate when

$$\frac{D_{x_2}}{D_{x_1}} = \frac{D_{y_2}}{D_{y_1}}, \quad (14)$$

and
$$|\theta_{x_2} - \theta_{x_1}| = |\theta_{y_2} - \theta_{y_1}|, \quad (15)$$

with $D_{x_2} > D_{x_1}$ and $D_{y_2} > D_{y_1}$. Under this definition, combinations like $C(2b, 1b)$ and $C(1d, 2d)$ were also degenerate: the orientation differences took opposite signs ($|\theta_{1b} - \theta_{2b}| = |30^\circ|$ and $|\theta_{2d} - \theta_{1d}| = |-30^\circ|$), or these two combinations were of mirror symmetry.

Similarly, $C(x_1, x_2, x_3, x_4)$ and $C(y_1, y_2, y_3, y_4)$ were degenerate when

$$\frac{D_{x_j}}{D_{x_i}} = \frac{D_{y_j}}{D_{y_i}}, \quad \forall i, j = 1 - 4 \quad (16)$$

and
$$|\theta_{x_j} - \theta_{x_i}| = |\theta_{y_j} - \theta_{y_i}|, \quad \text{and } j > i \quad (17)$$

with $D_{x_j} > D_{x_i}, D_{y_j} > D_{y_i}$ for $j > i$. Degeneracy of each combination was defined as the number of combinations sharing the bump spacing ratio and orientation difference with itself. Figure S6D illustrates the degeneracy of each combination of four or two modules. On average, the combinations of four modules were much less degenerate than those of two modules.

Reliability of estimation

As mentioned above, the rank method worked well with small noise in grid spacing

and orientation recorded and combinational non-degeneracy. With relatively large noise or degeneracy, there might be a combination C_n satisfying both $CV(M_R, C_n) \leq CV(M_R, C_R)$ and $\Delta O(M_R, C_n) \leq \Delta O(M_R, C_R)$, which would result in an incorrect estimate $C_E = C_n \neq C_R$ based on the rank method.

To assess the reliability of estimation, we calculated the probability of $C_R = C_m$ under the condition of $C_E = C_n$, i.e., $P(C_R = C_m | C_E = C_n)$. $P(C_R = C_n | C_E = C_n)$ reflects the reliability of estimation. In the presence of noise, the recorded grid modules M_R conferred by $C_R = C_m$ should obey

$$D_m^i / S_R^i = \alpha_m + \eta_m^i \quad i = 1 - 4 \quad (18)$$

and
$$\tilde{O}_R^i = (\pm\theta_m^i) + \varepsilon_m^i, \quad (19)$$

where η_m^i and ε_m^i denoted the noise in grid spacing and orientation. Given the noise strength, we calculated $P(C_E = C_n | C_R = C_m)$ by performing large numbers of simulations. It was further assumed that all C_m had the same chance to constitute grid modules, i.e., $P(C_R = C_m) = p$ ($m = 1 - 7315$). Then, we got $P(C_E = C_n \cap C_R = C_m) = P(C_E = C_n | C_R = C_m)P(C_R = C_m)$, $P(C_E = C_n) = \sum_m P(C_E = C_n \cap C_R = C_m)$, and

$$P(C_R = C_m | C_E = C_n) = \frac{P(C_E = C_n \cap C_R = C_m)}{P(C_E = C_n)} \quad (20)$$

with $m, n = 1 - 7315$.

For animal a with $M_R = M_a$ and $C_E = C_a$, we just needed to focus on $P(C_R = C_m | C_E = C_a)$. For simplicity, we only calculated the probability of the first 20 combinations with relatively small r . For each $C_R = C_m$, the noise strength was assumed to be comparable to its difference from M_a . That is, $\eta_m^i \sim N(0, \sigma_m^2)$, where σ_m equaled the standard deviation of $\frac{D_m^i}{S_a^i} - \langle \frac{D_m}{S_a} \rangle$ ($i = 1 - 4$) and ε_m^i 's were assumed to be random positive numbers satisfying $\sum_{i=1}^4 \varepsilon_m^i = \sum_{i=1}^4 |\pm\theta_m^i - \tilde{O}_a^i|$. 500 trials were taken for each $C_R = C_m$. After calculating all $P(C_E = C_a | C_R = C_m)$, $P(C_R = C_m | C_E = C_a)$ could be obtained according to Eq. (20).

References

Barry, C., Hayman, R., Burgess, N., and Jeffery, K.J. (2007). Experience-dependent rescaling of entorhinal grids. *Nat. Neurosci.* *10*, 682-684.

Góis, Z.H.T.D., and Tort, A.B.L. (2018). Characterizing speed cells in the rat hippocampus. *Cell Rep.* *25*, 1872-1884.

Gu, Y., Lewallen, S., Kinkhabwala, A.A., Domnisoru, C., Yoon, K., Gauthier, J.L., Fiete, I.R., and Tank, D.W. (2018). A map-like micro-organization of grid cells in the medial entorhinal cortex. *Cell* *175*, 736-750.

Hinman, J.R., Brandon, M.P., Climer, J.R., Chapman, G.W., and Hasselmo, M.E. (2016). Multiple running speed signals in medial entorhinal cortex. *Neuron* *91*, 666-679.

Kropff, E., Carmichael, J.E., Moser, M.-B., and Moser, E.I. (2015). Speed cells in the medial entorhinal cortex. *Nature* *523*, 419-424.

Stensola, H., Stensola, T., Solstad, T., Frøland, K., Moser, M.-B., and Moser, E.I. (2012). The entorhinal grid map is discretized. *Nature* *492*, 72-78.

Krupic, J., Bauza, M., Burton, S., Barry, C., and O'Keefe, J. (2015). Grid cell symmetry is shaped by environmental geometry. *Nature* *518*, 232-235.

Sun, C., Kitamura, T., Yamamoto, J., Martin, J., Pignatelli, M., Kitch, L.J., Schnitzer, M.J., and Tonegawa, S. (2015). Distinct speed dependence of entorhinal island and ocean cells, including respective grid cells. *Proc. Natl. Acad. Sci. U.S.A.* *112*, 9466-9471.